Strain Localization and Elastic-Plastic Coupling During Deformation of Porous Sandstone

Thomas A. Dewers[1*], Kathleen A. Issen[2], David J. Holcomb[1,3], William A. Olsson[1,3], and Mathew D. Ingraham[1]
[1]Sandia National Laboratories, Geomechanics Department, Albuquerque, NM
[2]Mechanical and Aeronautical Engineering, Clarkson University, Potsdam, NY
[3]Retired

November 11, 2013

*Corresponding Author:
Thomas Dewers
tdewers@sandia.gov
Sandia National Laboratories
P.O. Box 5800 MS 0751
Albuquerque, NM 87185
505 845 0631 (phone)
505 844 7354 (fax)

Abstract

Results of axisymmetric compression tests on weak, porous Castlegate Sandstone (Cretaceous, Utah, USA), performed at various mean stresses and covering a range of dilational and compactional behaviors, are examined for localization behavior. Assuming isotropy, bulk and shear moduli evolve as increasing functions of mean stress and Mises equivalent shear stress respectively, and as decreasing functions of work-conjugate plastic strains. Acoustic emissions events located during testing show onset of localization and permit calculation of observed shear and low-angle compaction localization zones, or bands, as localization commences. Total strain measured experimentally partitions into: A) elastic strain with constant moduli, B) elastic strain due to stress dependence of moduli, C) elastic strain due to moduli degradation with increasing plastic strain, and D) plastic strain. The third term is the elastic-plastic coupling strain, and though often ignored, contributes significantly to pre-failure total strain for brittle and transitional tests. Constitutive parameters and localization predictions derived from experiments are compared to theoretical predictions. In the brittle regime, predictions of band angles (angle between band normal and maximum compression) demonstrate good agreement with observed shear band angles. Compaction localization was observed in the transitional regime in between shear localization and spatially pervasive compaction, over a small range of mean stresses. In contrast with predictions, detailed acoustic emissions analyses in this regime show low angle, compaction-dominated localization.

1. Introduction

Sandstones exhibit a range of deformational responses under stress conditions typical of the earth's subsurface. Understanding these responses, and quantifying their behavior mathematically (i.e., constitutively), is necessary to predict sandstone response for a variety of sub-surface geo-engineering pursuits such as oil and gas production and exploration, and geologic carbon storage [*de Waal and Smits*, 1985; *Rutqvist et al.*, 2009, *Wawersik et al.*, 2000]. An important aspect of rate-independent sandstone deformation is the transition between localized deformation, in the form of shear and compaction zones or bands (i.e., concentrated tabular zones of strain that lack a discrete surface of discontinuity), and spatially pervasive pore collapse. The formation and development of localization can have important consequences for reservoir quality. Predictability of localized deformation from advanced constitutive modeling is thus a relevant consideration for waste injection or resource extraction [*Sulem et al*., 1999; *Sulem and Ouffroukh*, 2006; *Gajo and Bigoni*, 2008].

Localization in sandstones has been studied since the late 1970's [*Aydin*, 1978; *Aydin and Johnson*, 1983; *Antonellini and Aydin*, 1995], and recently identified variants in sandstone localization behavior include shear bands and compaction bands [*Olsson*, 2001; *Holcomb and Olsson*, 2003; *Wong et al*., 2001; *Klein et al*., 2001, *Issen and Rudnicki*, 2000; 2001; *Olsson et* *al*., 2002; *Detournay et al*., 2003; *Bésuelle et al.*, 2003; *Haimson*, 2001; 2003*; Borja and Aydin*, 2004; *Borja*, 2004; *Borja*, 2006; *Haimson and Lee*, 2004; *Baud et al*., 2004; *Tembe et al*., 2006; *Stanchits et al*., 2007; *Rudnicki*, 2007; *Eichhubl et al.*, 2010; *Ingraham et al*., 2013a; 2013b] and extension (dilation) bands [*Bésuelle et al*., 2000; *Bésuelle,* 2001*; Du Bernard et al*., 2002]. *Aydin et al*. [2006] note that the earliest reports of compaction bands in the field were by *Hill* [1989], and possibly the first experimental evidence of compactional deformation bands produced in the laboratory were by *Muhuri* [1994]. Recent detailed descriptions by *Eichhubl et al*. [2010] discern between pure compaction bands and shear-enhanced compaction bands.

While it is desirable to link constitutive response of laboratory samples to field examples, the disparate time scales and complex boundary conditions existing in field settings versus experiments make such comparisons difficult [*Holcomb et al*., 2007]. As such, direct comparison of geological examples and laboratory experiments is fraught with uncertainty. It is relevant however to understand laboratory constitutive response in order to gain some insight on field observation. In axisymmetric compression experiments ($\sigma_1 > \sigma_2 = \sigma_3$, where the principal stresses are $\sigma_1 \geq \sigma_2 \geq \sigma_3$, positive in compression), compaction localization has been observed to form in high porosity sandstones (20-28%) [*Olsson*, 1999; *DiGiovanni et al.*, 2000; *Olsson and Holcomb*, 2000; *Wong et al.*, 2001; *Klein et al.*, 2001; *Holcomb and Olsson*, 2003; *Baud et al.*, 2004; *Vajdova et al.*, 2004; *Stanchits et al.*, 2007]. Work by *Olsson* [1999], *Holcomb and Olsson* [2003] and *Vajdova et al*. [2004] demonstrate that localized compactive behavior results in order of magnitude changes in permeability.

This research examines mechanical response and localization behavior of a porous sandstone reservoir analogue rock, the Upper Cretaceous Castlegate Formation sandstone of east central Utah, USA [*McLaurin and Steel*, 2007], a dominantly fluvial sheet sand facies of the

Mesaverde Group. A suite of axisymmetric compression tests are conducted over a wide range of mean stresses under triaxial and constant-mean stress loading conditions. While compaction localization is of particular interest, Castlegate samples are also observed to fail via shear localization or uniform (non-localized) pore collapse, depending on mean stress. The localization theory of *Rudnicki and Rice* [1975] is applied toward predicting observed failure modes, and focus is placed on elastic-plastic coupling (i.e., modulus degradation with plastic strain) as an important consideration for constitutive modeling of porous sandstone deformation.

2. Theoretical Background

2.1 Constitutive Response and Elastic-Plastic Coupling

To evaluate localization predictions from *Rudnicki and Rice* [1975], the total strain determined in experiments must be separated into elastic and inelastic components. This section describes the model used to conduct this strain separation. We start with common assumptions in elastic-plastic constitutive models, namely the separation of total strain into elastic and plastic parts (denoted by '*e*' and '*p*' superscripts)

$$\varepsilon_{ij}^{t} = \varepsilon_{ij}^{e} + \varepsilon_{ij}^{p} \qquad (1)$$

where, upon unloading to zero stress, elastic strain vanishes and total strain equals plastic strain. We additionally assume an elastic strain that follows from

$$\sigma_{ij} = C_{ijkl}\varepsilon_{kl}^{e} \qquad (2)$$

With assumptions of isotropy and with usual definitions of invariants, (2) becomes

$$\varepsilon^e = \frac{\sigma}{K}\,, \quad \gamma^e = \frac{\tau}{G} \qquad (3)$$

For the axisymmetric compression (ASC) tests used here, mean stress $\sigma = -I_1/3 = -\sigma_{kk}/3$ is determined by $\sigma = (\sigma_A + 2\sigma_L)/3$ and Mises shear stress, $\tau = \sqrt{J_2} = \sqrt{\tfrac{1}{2} s_{ij} s_{ij}}$, (where I_1 and J_2 are the first and second invariants of the stress tensor, and the deviatoric stress is $s_{ij} = \sigma_{ij} - \tfrac{1}{3}\sigma_{kk}\delta_{ij}$) is given by $\tau = (\sigma_A - \sigma_L)/\sqrt{3}$, $\sigma_A = \sigma_1$ is the axial stress and $\sigma_L = \sigma_3 = \sigma_2$ is the confining pressure. The elastic volumetric strain is found from $\varepsilon^e = \varepsilon_A^e + 2\varepsilon_L^e$, and the elastic shear strain from $\gamma^e = 2\left(\varepsilon_A^e - \varepsilon_L^e\right)/\sqrt{3}$, during elastic portions of deformation, where ε_A is the axial strain and ε_L is the lateral strain. The bulk modulus and shear modulus are K and G, respectively.

Guided by experimental behavior shown later, we examine stress and plastic strain dependence of elastic moduli as the following

$$K = K(\sigma,\varepsilon^p)\ , G = G(\sigma,\tau,\gamma^p) \qquad (4)$$

Placing these into the former relations and expressing in incremental form, these become

$$d\varepsilon^t = d\left(\frac{\sigma}{K(\sigma,\varepsilon^p)}\right) + d\varepsilon^p$$

and (5)

$$d\gamma^t = d\left(\frac{\tau}{G(\tau,\gamma^p)}\right) + d\gamma^p$$

Expanding the total derivative yields

$$d\varepsilon^t = \frac{d\sigma}{K} - \frac{\sigma}{K^2}\left(\frac{\partial K}{\partial \sigma} d\sigma + \frac{\partial K}{\partial \varepsilon^p} d\varepsilon^p\right) + d\varepsilon^p$$

and (6)

$$d\gamma^{t} = \frac{d\tau}{G} - \frac{\tau}{G^{2}}\left(\frac{\partial G}{\partial \tau}d\tau + \frac{\partial G}{\partial \gamma^{p}}d\gamma^{p}\right) + d\gamma^{p}$$

From this, there are four strain increments that we label

$$d\varepsilon^{A} = \frac{d\sigma}{K};\ d\varepsilon^{B} = -\frac{\sigma}{K}\frac{\partial K}{\partial \sigma}d\sigma;\ d\varepsilon^{C} = -\frac{\sigma}{K}\frac{\partial K}{\partial \varepsilon^{p}}d\varepsilon^{p};\ d\varepsilon^{D} = d\varepsilon^{p}$$

(7)

$$d\gamma^{A} = \frac{d\tau}{G};\ d\gamma^{B} = -\frac{\tau}{G}\frac{\partial G}{\partial \tau}d\tau;\ d\gamma^{C} = -\frac{\tau}{G}\frac{\partial G}{\partial \gamma^{p}}d\gamma^{p};\ d\gamma^{D} = d\gamma^{p}$$

where the superscript '*A*' refers to strain due to change in stress at a constant modulus, '*B*' is due to the stress dependence of the modulus, '*C*' is the coupled strain due to plastic strain dependence of the modulus, and '*D*' is the plastic strain. Strains *A*, *B* and *C* are mechanically recovered upon unloading to zero stress, and only strain *D* (plastic) is not recovered.

Following *Rudnicki* [1984], we distinguish between an "increment of inelastic strain" which arises from only irrecoverable (plastic) strain,

$$d\varepsilon^{P} = d\varepsilon^{D} \text{ and } d\gamma^{P} = d\gamma^{D}, \qquad (8)$$

versus an "inelastic increment of strain" that includes both irrecoverable plastic strain and strain arising from degradation of elastic moduli (and as such combines *C* and *D* strains). The inelastic increments of strain are required to evaluate localization predictions [*Rudnicki and Rice*, 1975; *Rudnicki* 1984]. Consistent with *Rudnicki* [1984] after *Hill and Rice* [1973], we use the following notation for inelastic increments of strain:

$$d^{P}\varepsilon = d\varepsilon^{C} + d\varepsilon^{D} \text{ and } d^{P}\gamma = d\gamma^{C} + d\gamma^{D} \qquad (9)$$

If the elastic moduli do not evolve with stress, then the *B* strain increment vanishes and (7) is equivalent to equation (2) of *Collins* [2002] and to equation (1) (with different sign convention) of *Rudnicki* [1984].

2.2 Localization Theory

The strain localization framework of *Rudnicki and Rice* [1975] predicts conditions for the onset of localization in the form of a planar band of deformation, consisting of shear parallel to the band and/or compaction or dilation normal to the band. Localization is attributed to a constitutive instability in an initially uniform, inelastic deforming, pressure-dependent material; formation of a planar band of localized strain is an alternative solution to continued homogeneous deformation. The localization condition was found to be $\det\left|n_i L_{ijkl} n_l\right| = 0$, where n_i are the components of the band normal and L_{ijkl} is the modulus tensor in the constitutive relation $d\sigma_{ij} = L_{ijkl} d\varepsilon_{kl}$. Using the localization condition, and assuming that the hardening modulus decreases with continued loading, *Rudnicki and Rice* [1975] determined the predicted band orientation and the expression for the critical hardening modulus. Here, we present the relevant expressions, specialized for axisymmetric compression testing. Shear bands are predicted when

$$-\sqrt{3} < \beta + \mu < +\sqrt{3}\left(\frac{2-\nu}{1+\nu}\right), \qquad (12)$$

where β is the dilation coefficient (local slope of the plastic potential, Figure 1), which is positive for dilatant response, and negative for compactant response. Values for the dilation coefficient are determined from inelastic increments of strain, $\beta = -d^{p}\varepsilon / d^{p}\gamma$, at the onset of localization. The friction factor is μ, which is the local slope of the yield surface (see Figure 1). At low to intermediate mean stresses, ${}^{p}\gamma$ is used to track yield surface evolution; therefore, the initial and subsequent yield surfaces are contours of constant ${}^{p}\gamma$. Values for μ are determined by calculating the local slope of the yield surface at the onset of localization. Poisson's ratio for elastic unloading is ν.

For shear bands, the predicted band angle is given by [*Rudnicki and Olsson*, 1998]:

$$\theta = \frac{\pi}{4} + \frac{1}{2}\arcsin\left[\frac{2}{3\sqrt{3}}\left(1+\nu\right)\left(\beta+\mu\right) - \frac{1}{3}\left(1-2\nu\right)\right], \tag{13}$$

where the band angle is defined as the angle between the band normal and the direction of maximum compression. The onset of localization is predicted to occur when the hardening modulus, *h*, (slope of the shear stress – plastic shear strain curve at constant mean stress) decreases to a critical value, h_{cr}. The expression for the critical hardening modulus for shear bands is [*Rudnicki and Rice*, 1975; *Issen and Challa*, 2008]

$$h_{cr}^{S} = \frac{G\left(1+\nu\right)}{9\left(1-\nu\right)}\left\{\left(\beta-\mu\right)^{2} - \frac{\left(1-\nu\right)}{2}\left[\sqrt{3}+\left(\beta+\mu\right)\right]^{2}\right\}. \tag{14}$$

If $\left(\beta+\mu\right) \le -\sqrt{3}$, then compaction bands, $\theta = 0°$, are predicted, and the expression for the critical hardening modulus is [*Issen and Rudnicki* , 2000]

$$h_{cr}^{C} = -\frac{4G\left(1+\nu\right)}{9\left(1-\nu\right)}\left(\beta+\frac{\sqrt{3}}{2}\right)\left(\mu+\frac{\sqrt{3}}{2}\right). \tag{15}$$

If $\left(\beta+\mu\right) \ge \sqrt{3}\left(2-\nu\right)/\left(1+\nu\right)$, then dilation bands, $\theta = 90°$ are predicted. However, since dilation bands were not observed in the Castlegate experiments described below, the expression for the hardening modulus is not provided, but can be found in other works [e.g., *Issen and Rudnicki*, 2000; *Issen and Challa*, 2008].

The above predictions are appropriate for low and intermediate mean stress tests, where significant plastic shear strain occurs. However, for high porosity sandstone, a yield surface cap exists [*Wong et al.*, 1992; *Wong et al.*, 1997; *Olsson*, 1999; *Baud et al.*, 2006; *Tembe et al.*, 1997, *Ingraham et al.*, 2013b] and under hydrostatic pressure, compaction is accompanied by significant plastic volume strain [*Zhang et al.*, 1990] and little plastic shear strain. Therefore, extending the yield surface as a contour of constant ${}^{p}\gamma$ to intersect the mean stress axis is problematic. A simple way to circumvent this problem is to formulate a separate constitutive framework for the cap, which depends on inelastic volume strain, instead of inelastic shear strain [e.g., *DiMaggio and Sandler*, 1971; *Issen*, 2002; *Baud et al.*, 2006]. To simplify our data analysis, we choose the cap model derived by *Issen* [2002], as the resulting localization conditions parallel those of *Rudnicki and Rice* [1975]. For the cap, the initial and subsequent yield surfaces are contours of constant ${}^{P}\varepsilon$; values for μ are still determined by calculating the local slope of the yield surface at the onset of localization. Determination of values for β remains unchanged. However, the relevant hardening modulus is now the "bulk" hardening modulus, *k*, (slope of the mean stress – plastic volume strain curve at constant shear stress). Using this cap mode, when β and μ are both negative (as expected for compacting material), equations (12) and (13) are still applicable. The critical bulk hardening modulus is $k_{cr} = h_{cr} / (\beta\mu)$, using the appropriate h_{cr} from equation (14) or (15) [*Issen*, 2002].

3. Experimental Methods

3.1 Axisymmetric Compression Experiments

There have been numerous studies examining deformation of Castlegate sandstone [*Vinegar et al*. 1991; *Olsson*, 1999; *Olsson and Holcomb*, 2000; *Olsson*, 2001; *Olsson* et al., 2002; *Holcomb and Olsson*, 2003; *Coop and Willson*, 2003; *Holcomb et al*., 2004; Ingraham et al., 2013a; 2013b], as it may serve as an outcrop analogue for porous reservoir sandstones from similar depositional environments. Here, an experimental data set of Castlegate behavior is compiled to compare localization occurrences to theoretical predictions. Coring, sample preparation and jacketing procedures were performed as described by *Olsson* [1999]. Right-cylindrical samples were prepared by coring parallel to the bedding plane and grinding to a nominal 5.08 cm diameter by 12.7 cm length. All samples were cored from the same block of Castlegate in an attempt to minimize sample-to-sample variability. As discussed by *Holcomb and Olsson* [2003], coring parallel to the bedding plane eliminates the possibilities that compaction bands are a product of variation in material properties across the bedding planes or simply collapse parallel to bedding.

The sandstone cylinders were jacketed with 100 micron copper foil, with a copper cap at each end. To minimize end frictional effects, a stearic acid-petroleum jelly lubricant was used between the copper cap and the sandstone, and a teflon sheet coated with molybdenum disulphide was placed between the outer copper caps and upper and lower pistons [*Holcomb and Olsson*, 2003].

Experiments were conducted using a servo-controlled test frame under axial strain control at 10^{-5} to 10^{-6} s^{-1} nominal strain rates, using total axial strain as the control variable, to minimize effects of machine stiffness and to better control strain rates during localization. Axial strain (ε_A)

measurements were made via linear variable differential transformer (LVDTs) mounted end to end on the sample, and lateral strains (ε_L) were measured using a ring gage mounted near the middle of the sample. Axial load was measured via an external load cell. During each loading path, mechanical data acquired include axial load, axial displacement, confining pressure, pore pressure (where applicable), radial displacement, and acoustic emissions. Stress states for samples deformed to large strains and higher mean stresses were corrected for changes in cross sectional area; for all samples that underwent localization, this correction amounts to less than 1 MPa and so was not applied in these cases.

Samples were subjected to a variety of loading paths: uniaxial, hydrostatic, hydrostatic followed by triaxial compression, and hydrostatic followed by constant mean stress loading. Seventeen experiments, consisting of these different loading paths, are summarized in Table 1. Results of seventeen such experiments are plotted in Figure 2, which shows axial stress – axial strain and – lateral strain behavior (in each of Figure 2A and B, the curves to the right plot axial strains, while the curves to the left plot lateral strains). These experiments are also portrayed in τ – σ stress space (Figures 2C-D). Figure 2A and C are for tests which exhibited some form of localization, while Figures 2B and D show results of tests which did not experience any localization behavior.

In most of the constant mean stress tests and in the uniaxial tests, unloading-reloading cycles (visible as stress decreases in the curves in Figures 2A-B) were performed to track the evolution of elastic properties of the sandstone. This permitted quantifying the important role of plastic deformation in modifying elastic parameters (elastic-plastic coupling as discussed above). During typical unloading cycles, stresses were decreased by about 10% of expected peak stress (for unloading during constant mean stress tests, σ_L was increased as σ_A was decreased, so as to change only τ), before reloading and continuing the loading portion of the test. During unloading loops, stress and strain exhibit hysteresis as a result of the use of an external load cell. Friction between piston and piston seal (where the piston enters the pressure vessel) delays transmission of load from the loading system to the sample, both on unloading and reloading. To surmount this, only portions of unloading loops, wherein friction has been overcome, were used to infer elastic properties. Only pre-peak unloading-reloading cycles were used in determining elastic moduli evolution, as after peak stress is achieved (corresponding to onset of shear or compaction localization), sandstone specimens can no longer be reasonably approximated as homogeneous.

3.2 Acoustic Emissions

For the majority of the experiments, acoustic emissions (AE) were recorded using arrays of three to fourteen transducers soldered to the sample copper jacket, in the manner described by *Olsson and Holcomb* [2000]. AE signals were amplified by 60 db in the frequency band from 100 kHz to 1.2 MHz. A full wave form recording system capable of acquiring about 5 events per second recorded events detected by five or more transducers. Signals were digitized at 8 bit resolution and 32 MHz for later use in event location. It is estimated that the recorded events represent approximately 10% of the total event set. Recorded events were processed by means of “picker” software to determine arrival times for the signal from an event at each transducer, and the simplex algorithm of *Olsson and Holcomb* [2000] was used in determining locations from the first arrivals. A separate event counter system triggered by one event detector typically records several hundred thousand events during an experiment. Event locations were used to determine orientation of localization features.

4. Experimental Results

4.1 Stress-Strain Response

Examples of Castlegate behavior under different loading conditions are shown in Figure 3. Black lines plot axial stress – axial strain curves, while grey lines plot AE rate. Uniaxial loading behavior is shown in Figure 3A (experiment 41; no AE was recorded for this test), resulting in a stress peak and formation of high-angle shear localization. Constant mean stress loading (σ equal to 30 MPa) is shown in Figure 3B (experiment 22), resulting in shear localization and a less distinct stress peak. Constant mean stress loading (σ equal to 70 MPa), with dominantly compactional localization is shown in Figure 3C (experiment 15). Constant mean stress loading (σ equal to 90 MPa, experiment 21), resulting in no localization, is shown in Figure 3D. Note that in Figures 3B-D, the initial loading curves contain a segment of hydrostatic loading, followed by an increase in differential stress at constant mean stress. The post-peak plateau in Figure 3C is characteristic of compaction localization and propagation [*Olsson and Holcomb*, 2000] and it is interesting that no stress drops are discernable along the stress plateau, as occur in other examples of experimental compaction localization [e.g. *Baud et al*., 2006].

In Figures 3B and C, it is evident in all experiments that some acoustic activity, suggestive of plastic deformation, initiated from the start of loading. Peak AE activity, for samples which underwent shear or compaction localization, occurs near peak stress (where localization commences as per *Olsson and Holcomb*, [2000]) and then tapers off. In experiment 21 (Figure 3D), in which no localization occurred, AE activity peaks near peak stress and dies off with subsequent loading, while in experiment 15 (compaction localization, Figure 3C), continued AE activity attends the development and propagation of zones of compaction localization. These results are consistent with the results of Ingraham et al. [2013].

4.2 Acoustic Emissions Analyses

Historically, determinations of localization were made post-test by measuring the slope of the macroscopic fracture, often made evident by the deformation of the jacket. For shear localization, this is reasonably valid because once shearing begins on a plane, it is difficult for the angle of localization to change due to the kinematic constraints of the now-discrete blocks of material sliding past each other. It is possible for other zones of localization to form, however, and then determination of initial bands of localization is impossible post-test. Because the localization analysis only applies at the point where the localization condition is first satisfied, it is important to know the band angle prior to significant deformation and possible formation of secondary features. The problem is compounded for low angle bands which often do not visibly deform the jacket or sample, requiring microscopic examination to determine localization band characteristics.

Acoustic emissions are elastic waves produced by grain-scale failures and motions that are assumed to be discrete microscopic sources of continuum macroscopic phenomena described by localization theories. If deformation is localized, then it follows that the locations where AE occurs should similarly be localized and can be used to track and characterize spatial character of the localization process. This technique has the advantage of being able to observe the interior of the sample during deformation without interfering with the experiment; it can detect features that are obscured or destroyed by the progressive deformation of the sample after localization occurs.

Deforming one specimen can easily result in 100,000 recorded AE, of which perhaps 50% can be located to an accuracy of 2-3 mm. By plotting the locations as a series of time slices, like a movie, the spatial and temporal evolution of the causative deformations can be observed. This was the approach used by *Olsson and Holcomb* [2000] to confirm that low angle zones of localized deformation, termed compactional bands by them, were forming and propagating through Castlegate sandstone. In that work, clouds of AE were described as relatively flat-lying, i.e., having a band angle of zero degrees. In the current work, a more thorough analysis was done of event cloud orientation to facilitate comparison with calculated band angles discussed later.

Figures 4, 5, and 6 are examples of AE results for tests, arranged in order of increasing mean stress, which produced shear localization, compaction localization, and no localization, respectively. In each figure, the lower panel plots axial stress as a function of axial strain, along with the band angle computed for the cloud of AE events that occurred during sequential time slices of the experiment. At the top of each figure are three examples, captured from the full results, showing the AE locations in the cylindrical specimen during three time slices, with a vector (in grey) showing the normal to the best fit plane. Black dots correspond to events in the upper half of the specimen that were used to compute the best-fit plane. Gray dots are events that occurred in the lower half of the specimen during the same time slice. Because localization frequently results in bands that are simultaneously forming in the top and bottom halves of the specimen, it was necessary to restrict the analysis to half of the sample at a time. Arrows pointing to the stress – strain curve indicate the portion of the test of which the examples are representative: pre-peak, near-peak and post-peak. In all figures, the plot has been rotated about the cylinder axis until the view direction is along the strike of the fitted plane, emphasizing the slope.

Results from a test at low mean stress, seen in Figure 4, show a diffuse band of events formed in the upper half of the sample near peak stress, and evolved post-peak into a band with a well defined slope. The band angle evolved from near 90°, a numerical artifact as discussed below, to about 50° as the stress dropped post peak. Near the stress peak, it is clear that AE activity had localized, but there was no obvious shear plane until the sample shortens by about 0.007 strain units post-peak. A possible explanation for this phenomenon is that when the localization condition is satisfied in the cylindrically symmetric stress state, the band angle with respect to the maximum principal stress is determined, but not the azimuthal angle. As a result, localization initiates on all possible planes with that band angle, resulting in a rotationally invariant cloud of events, which resolve into one dominant band as deformation continues.

A low angle compactional band formed in sample 15, which was tested at an intermediate mean stress (see Figure 5). Prior to peak stress, events were uniformly distributed with no meaningful band angle calculated. At peak, a well defined band formed near the upper end of the sample, accompanied by a nearly complete cessation of activity in the lower half of the sample. The band angle was computed to be approximately 10° and remained in the range of 5° to 15° as the band of AE activity propagated down the sample.

Figure 6 presents results for an experiment where no localization occurred. Pre-peak (left-most AE location plot), the events are uniformly distributed as would be expected for homogeneous deformation accompanied by plastic shear and volume strain associated with pore collapse. Near the peak (center plot) there is some indication of localization deformation as shown by the denser concentration of events in the lower half of the cylinder, but no real band or zone forms. As deformation continues, the event distribution becomes relatively uniform, consistent with the interpretation that localization did not occur in this sample. Note that no plane normal is plotted, even though the algorithms computed a good fit to a plane with a dip angle of approximately 90°, as shown in the lower portion of Figure 6. Visually it is clear that the best fit plane would indeed run parallel to the axis of the cylinder as a result of the 2.5 to 1 aspect ratio forced on the event cloud by the confines of the cylindrical specimen. However, for our purposes, this result is meaningless and attributable to sample geometry.

Acoustic emissions analyses were conducted for all specimens for which AE events were collected. For those specimens where localization occurred, the localization band angles were determined as described above; these observed angles are shown in Table 2. In some specimens, a low angle compaction localization developed at each end of the specimen; therefore, two angles are reported.

5. Strain Partitioning Into Elastic and Plastic Portions.

5.1 Evolution of Bulk Moduli

To examine evolution of elastic moduli with stress and plastic strain, we first look at Castlegate hydrostatic consolidation (experiment 38), shown in Figure 7A. The mean stress – volume strain curve portrays a typical behavior for porous sands and sandstones [*Zhang et al*., 1990; *Karner et al*., 2003; 2005], including an initial concave-up pressure-strain segment (nonlinear elastic), a first inflection followed by a slightly convex segment (initial and subsequent plastic yielding), a second inflection followed by a roll-over with large strain accumulation (pore collapse), and a final convex segment with increasing slope (compaction and pore crush-out). Four unloading loops and the final unloading segment in this experiment aid in interpreting elastic moduli evolution during the progressive loading. Evident by the difference in slopes of the initial loading and final loading segments is an increase in elastic compliance with accumulating plastic strain, that is, elastic-plastic coupling as discussed above.

For non-linear elasticity, it is important to distinguish between stress dependent secant moduli, such as given in (3), with tangent moduli, which are local slopes of stress-strain curves. We denote secant bulk and shear moduli as K and G respectively, and tangent bulk and shear moduli as K_{tan} and G_{tan}, respectively. Tangent bulk moduli, K_{tan}, are determined from local slopes of mean stress-volume strain curves in elastic loading/unloading regimes, which include pre-yield initial loading , during unload-reload cycles, and final unloading. For the initial, final, and unloading segments of the stress-strain curve for experiment 38 (Figure 7A), tangent moduli are plotted as symbols in Figure 7B. Values of K_{tan} increase initially due to stress dependence, and then decrease relative to the values of K_{tan} determined during the initial unloading loop, suggestive of plastic strain dependence due to yielding initiating at ~50 MPa. Combining the first unloading moduli with the pre-50 MPa moduli suggests a $K(\sigma)$ relation wherein K_{tan} increases as an exponential function of σ, similar to that determined for Berea sandstone by *Kahn et al.* [1991]. The K_{tan} calculated from the second unloading loop displays a slope that is less than values from the first unloading loop, as are moduli determined from the final unloading. Note that the final unloading moduli also indicate an exponential $K_{tan}(\sigma)$ relation, but with lesser slopes, suggesting that moduli at similar stress conditions decrease as a function of increasing plastic strain. Slopes and zero-stress intercepts appear to both decrease monotonically as a function of increasing plastic strain. These relationships are also found during hydrostatic loading/unloading portions of other experiments (not shown here).

In an attempt to capture these functional relationships in as simple and tractable a mathematical form as possible, we suggest the following for a stress- and strain-dependent bulk modulus, $K = K(\sigma, \varepsilon^{p})$:

$$K = K_0\left(1 + K_1\sigma - K_2 e^{-K_3 K_0 \sigma}\right) \qquad (16)$$

where K_1, K_2 and K_3 are constants and K_0 is a parameter that decreases as a function of plastic volume strain, ε^p. Here we have chosen the work-conjugate stress and strain variables (i.e., an increment of plastic work for an isotropic material given by $dW = \sigma d\varepsilon^p + \tau d\gamma^p$) to express the stress and strain dependence of *K*. This stress dependence is suggested from work on compression- and shear-wave velocities in porous sandstones. For example *Kaselow and Shapiro* [2004] provide a pore-scale interpretation in which the exponential term in (16) derives from compliant microcracks and cracked-shaped pores, and the linear term derives from more rounded pores; these are termed compliant and stiff porosity, respectively. The plastic volume strain dependence we apply is based on empirical observation of Castlegate behavior.

The form of K_{tan} applicable to elastic portions of stress – strain curves, which include initial loading, unload-reload cycles, and final unloading (whereupon the increment of plastic strain $d\varepsilon^p$ vanishes) can be found by combining (16) with the first of equations (6) and assembling terms such that $d\varepsilon^e = d\sigma/K_{tan}$, where

$$K_{tan} = \left\{ \frac{1}{K} - \frac{\sigma}{K^2} \left(K_0^2 K_2 K_3 e^{-K_3 K_0 \sigma} \right) \right\}^{-1} \qquad (17)$$

Values for the parameter set $\{K_0, K_1, K_2, K_3\}$ can be determined by either curve fitting secant moduli to (3) or tangent moduli to (6). The procedure we adopt is to (1) fit the final unloading curve (Fig. 7A) to find $\{K_0, K_1, K_2, K_3\}$, and then fit unload-reload cycles with these values of K_1, K_2, and K_3 to find a unique K_0 applicable to each cycle and initial loading; and (2) determine a smooth function for $K_0 = f(\varepsilon^p)$ to interpolate between unload loops. As ε^p is initially unknown, a simple procedure for interpolation is to first find $K_0 = f(\varepsilon^t)$, that is, as a function of total strain. While there are certainly a number of functions that we could use, a simple form for K_0 that we have found to apply to all experimental results presented here is

$$K_0 = K_0'\left(1 - K_4 e^{-K_5/\varepsilon_p}\right) \quad (18)$$

where, for initial interpolating, the ε^p is replaced by ε^t. This expression is applied to each experiment with the same values for K_1, K_2, K_3, K_4, K_5 and a K_0 that evolves monotonically with plastic volume strain but is constant during unloading loops. Best-fit K_i parameters for initial loading, unload-reload cycles, and final unloading for non-localized samples are determined for each experimental mean stress-volume strain path (that is, we fit the secant modulus) by applying the nonlinear Levenberg-Marquardt regression algorithm, using a commercially available software package. To determine plastic volume strains applicable to a given unloading loop, each unloading stress – strain curve is extrapolated to zero stress, and the plastic volume strain is equated to the intercept of the volume strain axis.

To demonstrate the viability of our model for K, calculated tangent moduli are shown as the solid black line in Figure 7B for experiment 38 using the parameterization scheme as {K_0', K_1, K_2, K_3, K_4, K_5} equal to {2814, 0.0057, 0.79, 1.54e-5, 0.98, 0.067}. Compared to experimental values (symbols in Figure 7B), this model for K_{tan} does well at the latter portions of the experiment and for initial loading, but slightly overestimates moduli for the second unload loop, and a slightly lessened slope for the first unload loop. For comparison, the calculated secant moduli K for the same K_i values is shown by the grey line in Figure 7B; values of the secant moduli are approximately half those of the tangent moduli for much of the stress path.

5.2 Partitioning of Total Volume Strain Into Elastic and Plastic Parts

Having developed a model for the evolution of K during loading and plastic yielding, it is a simple matter to calculate elastic volume strains by combining equations (3), (16) and (18), and, by subtracting elastic from total strains, to calculate plastic volume strain. This is shown graphically in Figure 7C. The solid black line is total (measured) volume strain, the dark grey line is calculated elastic strain ($\varepsilon^A+\varepsilon^B+\varepsilon^C$), and, by difference, the dashed black line shows plastic volume strain (ε^D). The light grey line, which shows no hysteresis, plots the elastic strain that would manifest if no modulus degradation occurred ($\varepsilon^A+\varepsilon^B$). It is immediately evident that elastic-plastic coupling (ε^C, the difference between the dark grey and light grey curves), caused by the plastic volume strain dependence of the bulk modulus, accounts for approximately half of the total strain for much of the loading path. Similar results were found for some lithofacies of the Mt. Simon Sandstone [*Dewers et al.*, 2013]. For example, at peak mean stress of 400 MPa, the total measured strain (ε^t) is about 0.18 strain units, plastic strain (ε^D) is about 0.05 strain units, and the elastic volume strain ($\varepsilon^A+\varepsilon^B+\varepsilon^C$) is 0.14 strain units. The elastic strain with no modulus degradation ($\varepsilon^A+\varepsilon^B$) would amount to a little less than 0.05 strain units, which implies that the coupling elastic strain (ε^C) and inelastic strain ($^{p}\varepsilon = \varepsilon^C+\varepsilon^D$) would, at peak load, amount to approximately 0.09 and 0.14 strain units, respectively. The coupling strain then, accounts for a significant portion of total strain accumulated during the experiment, as well as much of the shape of the overall hydrostat.

Figure 7D plots equation (18) as a dashed line, for the plastic strain path shown in Fig. 7C; the solid symbols are plotted for each unload-reload cycle. This suggests that much of the modulus degradation, with largest drop in modulus value, occurs between the second and third unload-reload cycle. This is reasonable, corresponding to the largest accumulation of plastic strain and accordingly, the “knee” of the hydrostat. Values for $\{K_4, K_5\}$ applicable to using ε^p are {0.68, .003}.

5.3 Evolution of Shear Moduli and Partitioning of Total Shear Strain

Secant and tangent shear moduli, G and G_{tan}, can found by similar methods as done for bulk moduli. As an example we show evolution of shear moduli as functions of plastic shear strain, γ^p, and shear stress, τ, for experiment 42, a constant mean stress test at σ equal to 150 MPa. The stress path for 42 (Figure 8A) includes hydrostatic loading to 150 MPa, followed by a constant mean stress loading to τ equal to 70 MPa with eight unload loops. Sample 42 experienced no localization, which enable us to determine shear moduli from final unloading as well.

Figure 8B shows tangent moduli from the unload loops and final unloading, and is suggestive of a shear modulus that increases with τ at constant plastic shear strain, and decreases as a function of plastic shear strain, γ^p. (Note that we observe a clear mean stress dependence of shear moduli, but as most of our results are for constant mean stress tests, we focus on the observed shear stress dependence.) In analogy with our model for K, we choose to express the stress and plastic strain dependence of G in terms of the work-conjugate variables γ^p and τ as the following:

$$G = G_0^{'}\left(1 + G_4 e^{-G_5/\gamma_p}\right)(1 + G_1\tau)\,. \tag{19}$$

G_0 and G_1 parameters are determinable via a non-linear regressions procedure as was done for K. We initially fit the stress dependence from the final unloading to give G_1, as well as final G_0, and then apply the same G_1 to the unload loops. As was done in the case of bulk moduli, we first use the total strain in (19), replacing γ^p with γ^t, as a function that allows us to interpolate between unload loops. In Figure 8B, we compare calculated G_{tan} (symbols) to (19) using the parameterization scheme of {G_0', G_1, G_2, G_4, G_5} equal to {7611, 0.0071, 0.60, 0.0021} with overall good agreement.

By combining (3) with (19), we then calculate elastic shear strains (γ^A+γ^B+γ^C) shown by the dark gray line in Figure 8C, and then by difference with total strain, the plastic shear strain γ^p (or γ^D) shown by the dashed black line in Figure 8C. The calculated elastic strain (γ^A+γ^B) with no plastic strain dependence (i.e., G_4, G_5 in equation 19 equal to zero) is shown by the light grey line. In contrast with the hydrostat in Figure 7A, it is evident that plastic shear strain dominates measured values compared to the elastic strain, and the elastic strain associated with elastic plastic coupling (γ^C; the light grey curve subtracted from the dark grey curve) is roughly twice that of elastic strain with no coupling (γ^A + γ^B).

Evolution of the G_0 parameter with plastic shear strain γ^p is shown in Figure 8D. As was seen Figure 7C for the hydrostatic case, the biggest drop in shear modulus is associated with the "knee" of the stress strain curve, corresponding to the accumulation of plastic shear strain between the second and fourth unload-reload cycle.

5.4 Partitioning of Strain for Experiments Resulting in Localization

Following the procedures in the last two sections, results of partitioning of total strain into elastic and plastic portions for three experiments, up to peak stress where localization commenced, are shown in Figures 9A-F. These are experiment 41 (Figures 9A-B), loaded under uniaxial conditions to a peak τ of 8.7 MPa; experiment 22 (Figures 9C-D), loaded to 25 MPa mean stress hydrostatically, and then loaded to a peak τ of ~28 MPa at constant mean stress; and experiment 15 (Figures 9E-F), loaded to a mean stress of 70 MPa hydrostatically and then under triaxial conditions to a peak τ of ~50 MPa. Solid black lines in Figure 9 refer to total strain, dashed lines plot calculated plastic strains (ε^D and γ^D) , dark grey lines plot elastic strains including elastic-plastic coupling (ε^A+ε^B+ε^C and γ^A+γ^B+γ^C), and light grey lines are elastic strains ignoring the coupling strain terms ($\varepsilon^A+\varepsilon^B$ and $\gamma^A+\gamma^B$). In all three cases, changes in bulk moduli accompanying plastic volume strain were deemed so small as to be negligible, and were ignored in the calculation of plastic volume strain. However, elastic-plastic coupling in the determination of elastic shear strain was found to be extremely important (γ^C is roughly 25%, 50% and 66% of the total strain for experiments 41, 22 and 15, respectively), suggesting that a significant amount of pre-peak shear deformation in porous sandstones is attributable to elastic-plastic coupling. This observation also applies to experiments conducted at higher mean stresses which experienced no localization, although we do not include these results here.

This strain partitioning procedure was applied to eleven experiments which experienced localization (these are 3, 8, 13, 14, 15, 16, 17, 20, 22, 40, and 41 in Table 1 and Figure 2A and C) and two experiments at higher mean stress which exhibited no localization (these are 21 and 42 in Table 1 and Figure 2B and D). The partitioned *A*, *B*, *C*, and *D* volume and shear strains so calculated, and in particular the inelastic strains (*C*+*D*), are then used in determining constitutive parameters β and μ, needed to evaluate localization theory predictions in the next section. Note that the triaxial experiments 13, 17, and 3 had no unload-reload cycles from which to determine the evolution of *G*, so we applied the $G(\tau,{}^p\gamma)$ parameterization from 15 to these tests. As these were triaxial tests and as such cover a range of mean stress, this likely introduces some degree of uncertainty in strain partitioning for these experiments as *G* is a function of σ as well as τ.

6. Comparison with Localization Theory

6.1 Calculating μ: Yield Surfaces as Contours of Constant ${}^p\gamma$ and ${}^p\varepsilon$

As discussed in Section 2, predictions of localization as per *Rudnicki and Rice* [1975] depend on values of the constitutive parameters β, μ, and hardening modulus *h*. *Holcomb and*

Rudnicki [2001] determined yield surfaces as contours of plastic shear strain, γ^p; analogously, we use contours of inelastic shear strain, ${}^p\gamma$, which accounts for elastic-plastic coupling. Yield cap surfaces are determined as contours of inelastic volume strain, ${}^p\varepsilon$, in analogy with *Issen's* [2002] use of plastic volume strain ε^p, but accounting for elastic-plastic coupling. In this section we calculate μ as local slopes of shear and cap yield surfaces at peak stress conditions, where localization occurs.

For the shear surface, it is first necessary to determine a failure surface as the loci of peak loading stress conditions. These are shown in Figure 10A (black squares) for five experiments that displayed localization. A non-linear mean stress-dependent failure surface suggested by *Brannon et al.* [2009] fits the peak stress data to an excellent degree, as shown by the dashed line in Figure 10A (corresponding to {a_1, a_2, a_3, a_4} equal to {48, 0.03, 46, 0.096}):

$$\tau = a_1 - a_3 e^{-a_2\sigma} + a_4\sigma \qquad (20)$$

This implies a value of μ equal to

$$\mu = \frac{\partial\tau}{\partial\sigma} = a_2 a_3 e^{-a_2\sigma} + a_4 \qquad (21)$$

For shear yield surfaces that apply to localization (i.e., at peak stresses) we are looking for contours of constant ${}^p\gamma$ that asymptote at the peak stress for the experiment of interest, in order to calculate slopes and μ for that experiment. Thus we apply the same form of (20) but fit contours of ${}^p\gamma$ that apply to the value of ${}^p\gamma$ at failure (localization). Results for four experiments (only results for 41, 22, 20, and 15 are shown for clarity in plotting) are shown in Figure 10A. Corresponding values of μ found from the curve fits and (21) are given in Table 2.

Similarly, for cap surfaces, we seek an elliptical-like equation to fit as contours of constant inelastic volume strain ${}^p\varepsilon$. We follow the form used by *Brannon et al.* [2009]:

$$\tau = \tau_f \left\{ 1 - \frac{\sigma - \sigma_f}{\sigma_h - \sigma_f} \right\}^{\frac{1}{2}} \qquad (22)$$

where σ_f and τ_f are equal to mean stress and shear stress values at the intersection of the cap surface with the failure surface and σ_h is the mean stress where the cap intersects the hydrostat. To express the cap surface as a contour of constant ${}^p\varepsilon$, we apply (22) with τ_f and σ_f as fit parameters using values of σ_h determined experimentally. The results for 14 and 15, experiments which failed at higher mean stresses via a low-angle compaction localization (i.e., as shown in Figure 5B for 15), and 21, which experienced no localization (as shown in Figure 5C), are shown in Figure 10B. The μ value is calculated as the slope of (22) where the cap meets the failure surface, found from (22) to be:

$$\mu = \frac{\partial \tau}{\partial \sigma} = \frac{\tau_f}{2} \left\{ 1 - \frac{\sigma - \sigma_f}{\sigma_h - \sigma_f} \right\}^{-\frac{1}{2}} \left\{ \frac{1}{\sigma_h - \sigma_f} \right\} \qquad (23)$$

Corresponding values of μ for the cap yield surface are given in Table 2 for 14, 13, 15, 17, and 21. Samples 13 and 17 experienced localization at nearly the same ${}^p\varepsilon$ values as 15 (0.0050 and 0.0055 for 13 and 17, respectively, compared to 0.0044 for 15), so we apply the slope determined from 15 to these experiments.

6.2 Calculating the β Constitutive Parameter

The dilation coefficient is a function of inelastic increments of volume and shear strain as per *Rudnicki and Rice* [1975] and *Rudnicki* [1984] and is given by $\beta = -d\,{}^p\varepsilon / d\,{}^p\gamma$. The β value is found from local slope of inelastic strain ${}^p\varepsilon$ versus ${}^p\gamma$ plot at peak stress, approximately when localization commences. Recall that inelastic strains as defined here include the C and D components of strain. Plots of ${}^p\varepsilon$ versus ${}^p\gamma$ for experiments 40, 41, 22, 20, 14, 15, 17, 13, 3 and

21 (in order of increasing mean stress) are shown in Figure 11. Values of β at peak load are given in Table 2.

Experiments that experienced shear localization (40, 41, 22, and 20) show failure at progressively larger values of ${}^{p}\gamma$, with decreasing positive values of β, correlated to increasing mean stress. Experiments that experienced compaction localization have increasingly negative values of β that correlate with increasing values of ${}^{p}\varepsilon$. Sample 21, which did not experience localization, is a constant σ test conducted at higher values of σ than the other tests, and so experienced more ${}^{p}\varepsilon$ along the initial hydrostatic loading portion. This is why that experiment shows a higher ${}^{p}\varepsilon$ value at the zero-${}^{p}\gamma$ intercept than the other tests. Sample 3 is a triaxial experiment that localized at the highest σ of any of the other experiments that exhibited compaction localization. Between the σ values for samples 3 and 21 (between 80 and 90 MPa) there is a transition in behavior from compaction localization to pervasive compaction. Between the σ values for samples 20 and 14 (between 30 and 50 MPa), there is a transition in behavior from shear band localization to compaction localization.

6.3 Predicted Band Angles and Hardening Moduli h_{cr}

Results of β and μ calculated for the eleven localizing samples of Figure 10A and B and Figure 11, plus the non-localizing experiment 21 for comparison, are given in Table 2, along with the shear modulus and calculated Poisson's ratio (found from $\nu = (3K - 2G) / [2(3K + G)]$), both determined just pre-peak. These values of β and μ are, to our knowledge, the first to be determined using the full increment of inelastic strains and allowing for elastic-plastic coupling.

Critical hardening moduli for the shear surface, equations (5) and (6), and for the cap surface (where $k_{cr} = h_{cr} / (\beta\mu)$ after *Issen* [2002]), using equations (5) and (6)), are given in Table 2 for the localizing experiments, along with the predicted band angles from equation (4).

7. Discussion

Observed angles of shear banding and compaction localization are given in Table 2 and can be compared to predicted band angles from the Rudnicki and Rice (1975) formalism, also shown in Table 2. The two uniaxial tests (40 and 41) formed shear bands at angles of 67° – 70° (Table 2). The overall specimen response was dilatant ($\beta \approx 0.92$ and 1.01 for 41 and 40 respectively) and the predicted band angles for both tests are 73 - 76°. The two constant mean stress tests at low mean stress (specimens 20 and 22) formed shear bands at angles of 30° – 48°. The response was still dilatant ($\beta \approx 0.17$ and 0.26 for 20 and 22 respectively), but less so than the uniaxial tests, and the predicted band angles are 49° and 50°. Thus, at low mean stresses, the predicted shear band angle demonstrates reasonable agreement with observed band angles, although predicted band angles are consistently slightly larger than observed angles. However, the predicted critical hardening modulus is strongly negative, in contrast with the observation of localization at/near peak stress, where $h \approx 0$. Predicted band angles for compactant experiments 14, 13, 15, 17, and 21, with negative values of β and values of μ calculated using shear yield surfaces as contours of constant ${}^{p}\gamma$, consistently over-predict band angles (35-40^{o} compared to 4-25^{o} as observed). Band angles predicted using the cap surfaces as contours of constant ${}^{p}\varepsilon$, shown in the lower portion of have overall better agreement (10-23^{o} calculated compared to 4-25^{o} observed). Unlike the shear band tests, for compaction localization, the predicted critical hardening moduli are all positive, but this still contrasts with the observation of localization at/near peak stress, where $h \approx 0$. There is one transitional specimen (14), at 50 MPa mean stress, that exhibited overall compactant response ($\beta = -0.23$) for a predicted band angle of 40°. This specimen formed a low angle band, 8° – 12°, even though the overall response was less compactant than the experiments exhibiting compaction localization.

As expected and as observed by others, at higher mean stresses beyond a threshold value, no localization occurs. This threshold is approximately 90 MPa for the Castlegate specimens in this study. At this mean stress, the overall response was compactant, with β equal to –0.51, but this value is much less than experiments at slightly lower mean stresses (70-79 MPa) that did exhibit compaction localization. Therefore, there appears to be a relatively small range of intermediate mean stresses for which the material response becomes strongly compactant leading to compaction localization. Below this small range, shear bands form and above it no localization occurs.

8. Summary and Conclusions

A suite of axisymmetric compression tests ($\sigma_1 > \sigma_2 = \sigma_3$) were presented over a wide range of mean stresses and deformational behaviors, for Castlegate sandstone, an analog for porous sandstone reservoirs for oil production or subsurface carbon storage. Results were used to develop a complete set of constitutive parameters, including stress and plastic strain dependence of the elastic moduli. Acoustic emissions (AE) events were utilized to identify strain localization. Constitutive parameters and AE results permitted evaluation of theoretical predictions for strain localization.

At low mean stress, shear localization occurred, while at high mean stress, homogeneous compaction without localization (pore collapse) was observed. At a small range of intermediate mean stresses, compaction localization develops. For localization modes, acoustic emissions events confirmed that band formation generally begins at/near the peak in the axial stress – axial strain curve and enabled determination of localization band angle. For shear bands, the observed band angles (angle between the band normal and the direction of maximum compression) were 30° – 70°, and decreased with increasing mean stress. For intermediate stress tests, compaction localization occurred. Previously this localization mode was reported as compaction bands (theoretically, a pure compaction band angle is 0°). However, the more detailed AE analyses performed in this work reveals that these features are actually low angle bands, 4° – 25°; the lack of shear offset suggests that they are dominantly compactant. These observed angles were used to evaluate theoretical predictions using the framework of *Rudnicki and Rice* [1975].

An important finding is the relative importance of elastic-plastic coupling via the plastic strain dependence of elastic moduli in Castlegate Sandstone elastic-plastic deformation. Bulk and shear moduli evolve as increasing functions of mean stress and Mises equivalent shear stress, respectively, and as decreasing functions of the work-conjugate plastic strains. Total strain increments were partitioned into four parts: A) elastic strain (constant moduli), B) strain due to stress dependence of elastic moduli, C) strain due to moduli degradation with increasing plastic strain ("coupling strain"), and D) plastic strain. The sum of the first three parts is the elastic strain increment; the plastic strain increment, part *D*, is total strain less elastic strain. The sum of the third and fourth parts (*C* and *D*) is referred to as the increment of inelastic strain, and was used in the calculation of constitutive parameters. The friction factor, μ, is the slope of the yield surface, which is a contour of constant inelastic shear strain (for the cap, μ is determined as a contour of constant inelastic volume strain). The dilation coefficient, β, is the negative of the slope of the inelastic volume strain – inelastic shear strain curve.

At low mean stresses, overall specimen response was dilatant ($\beta > 0$) and the predicted range of band angles of 40° – 73° are in good agreement with observed band angles of 30° – 70°, although predicted angles were consistently slightly higher than the observed. At intermediate mean stresses, the response was compactant ($\beta \approx -0.5$) and observed band angles were 4° – 25°. Using a shear yield surface calculated as a contour of inelastic shear strain, the yield surface slope is positive and predicted band angles were 35° – 40°; this procedure thus over-predicted band angles significantly. Alternatively, using a cap yield surface calculated as a contour of inelastic volume strain, the yield surface slope is negative and lower angle bands were predicted ($10^o – 23^o$), in better agreement with observed values. At low mean stresses, the predicted critical hardening modulus is strongly negative (implying post-peak localization), while for intermediate mean stresses, it is positive (pre-peak localization); these both contrast with AE results, which show that localization occurs at/near peak stress where the hardening modulus is zero.

In conclusion, the *Rudnicki and Rice* [1975] theoretical treatments show a reasonable predictive ability with respect to Castlegate Sandstone deformation. Elastic-plastic coupling is an important consideration for constitutive behavior of weak porous sandstones, and can be a major component of elastic-plastic behavior in constitutive modeling for subsurface engineering endeavors.

Acknowledgements

The authors gratefully acknowledge funding from the U.S. Department of Energy, Office of Science, Basic Energy Sciences Program and the National Science Foundation Award EAR-0711346 to Clarkson University (for KI). We thank Tom Pfeifle and Joe Bishop for comments and their work on improving the manuscript, and Rebecca Brannon for championing our work on elastic-plastic coupling. Sandia National Laboratories is a multi-program laboratory managed and operated by Sandia Corporation, a wholly owned subsidiary of Lockheed Martin Corporation, for the U.S. Department of Energy's National Nuclear Security Administration under contract DE-AC04-94AL85000.

References

Antonellini, M., and A. Aydin (1995), Effect of faulting on fluid flow in porous sandstones: geometry and spatial distribution, *American Assoc. Petrol. Geol. 79*, 642–671.

Aydin, A. (1978), Small faults formed as deformation bands in sandstone, *Pure and Applied* Geophysics 116, 913–930.

Aydin, A., and A. M. Johnson (1983), Analysis of faulting in porous sandstones, *J. Struct. Geol. 5*, 19–31.

Aydin, A., R.I. Borja, and P. Eichhubl (2006), Geological and mathematical framework for failure modes in granular rock, *Journal of Structural Geology 28*, 83-98

Baud, P., E. Klein, and T.-f. Wong (2004), Compaction localization in porous sandstones: spatial evolution of damage and acoustic emission activity, *Journal of Structural Geology 26*, 603-624.

Baud, P., V. Vajdova, and T.-f. Wong (2006), Shear-enhanced compaction and strain localization: Inelastic deformation and constitutive modeling of four porous sandstones, *J. Geophys. Res.*, 111, B12401, doi:10.1029/2005JB004101.

Bernabe', Y., D. Fryer, and R. Shively (1994), Experimental observations of the elastic and inelastic behaviour of porous sandstones, *Geophys. J. Int., 117,* 403-418.

Bésuelle, P. (2001), Compacting and dilating shear bands in porous rock: theoretical and experimental conditions, *J. Geophys. Res., 106*, 13435–13442.

Bésuelle, P., J. Desrues, and S. Raynaud (2000), Experimental characterisation of the localisation phenomenon inside a Vosges sandstone in a triaxial cell, *Int. J. Rock Mech. Min. Sci.*, *37,* 1223-1237.

Bésuelle, P., P. Baud, and T.-f. Wong (2003), Failure mode and spatial distribution of damage in Rothbach Sandstone in the brittle-ductile transition, *Pure Applied Geophysics 160*, 851-868.

Borja, R. (2006), Conditions for instabilities in collapsible solids including volume implosion and compaction banding, *Acta Geotechnica, 1*:107-122, DOI 10.1007/s11440-006-0012-x.

Borja, R., and A. Aydin (2004), Computational modeling of deformation bands in granular media. I. Geological and mathematical framework, *Comput. Methods Appl. Mech. Engrg. 193*, 2667-2698.

Borja, R. (2004), Computational modeling of deformation bands in granular media. II: Numerical simulations, *Comput. Methods Appl. Mech. Engrg. 193*, 2699-2718.

Brannon, R.A., A.F. Fossum, and O.E. Strack (2009) KAYENTA: Theory and User's Guide. Sandia National Laboratories, SAND2009-2282. Albuquerque, NM.

Collins, I., and G. Houlsby (1997), Application of thermomechanical principles to the modeling of geotechnical materials, *Proc. R. Soc. Lond. A, 453*, 1975-2001.

Collins, I. (2002), Associated and non-associated aspects of the constitutive laws for coupled elastic/plastic materials. *The Int. J. of Geomechanics* 2, 259-267.

Coop, M., and S. Willson (2003), Behavior of hydrocarbon reservoir sands and sandstones, *J. Geotechnical and Geoenvironmental Eng. 129*, 1010-1019.

De Waal, J.A. and R.M.M. Smits (1985), Prediction of reservoir compaction and surface subsidence: Field application of a new model, *SPE Ann. Tech. Conf. & Exhib., 14214*, Las Vegas, NV.

Dewers, T.A., Newell, P., Broome, S., Heath, J., and S. Bauer (2013), Geomechanical behavior of Cambrian Mount Simon Sandstone reservoir lithofacies, *Int. J. Greenhouse Gas Control*, in press.

Detournay, C., P. Cundall, and J. Parra (2003), A study of compaction band formation with the double yield model, in *FLAC and Numerical Modeling in Geomechanics*: Proceedings of the Third International FLAC Symposium, edited by B. et Al., pp. 27–33, Swets & Zeitlinger.

DiGiovanni, A., J. Fredrich, D.J. Holcomb, and W. A. Olsson (2000), Micromechanics of compaction in an analogue reservoir sandstone, in *Proc. North American Rock Mech. Symp.*, edited by Girard, J., Liebman, M., Breeds, C. , and T. Doe, Balkema, pp. 1153-1158, July 13.

DiMaggio, F.L. and I.S. Sandler (1971), Material model for granular soils, *J. Eng. Mech. Div., ASCE, 97*, 935-950.

Du Bernard, X., P. Eichhubl, and A. Aydin (2002), Dilation bands: A new form of localized failure in granular media, *Geophys. Res. Lett., 29*(24), 2176, doi:10.1029/2002GL015966.

Eichhubl, P., J.N. Hooker, and S.E. Laubach (2010), Pure and shear-enhanced compaction bands in Aztec Sandstrone, *Journal of Structural Geology* doi:10.1016/j.jsg.2010.02.004.

Gajo, A., and D. Bigoni (2008), A model for stress and plastic strain induced nonlinear, hyperelastic anisotropy in soils, *Int. J. Numerical Analytical Methods in Geomechanics 32*, 833-861, doi:10.1002/nag.648

Gajo, A., D. Muir Wood, and D. Bigoni (2007), On certain critical material and testing characteristics affective shear band development in sand, *Geotechnique 57*, 449-461.

Haimson, B., and H. Lee (2004), Borehole breakouts and compaction bands in two high-porosity sandtones, *Int. J. Rock Mech. & Min. Sci., 41*, 287–301.

Haimson, B. C. (2001), Fracture-like borehole breakouts in high-porosity sandstone: are they caused by compaction bands?, *Phys. Chem. Earth (A), 26*, 15–20.

Haimson, B. C. (2003), Borehole breakouts in Berea sandstone reveal a new fracture mechanism, *Pure Appl. Geophys., 160,* 813–831.

Hill, R.E. (1989), Analysis of Deformation Bands in the Aztec Sandstone, Valley of Fire State Park, Nevada. M.S. thesis, University of Nevada, Las Vegas.

Hill, R. and J.R. Rice (1973), Elastic potentials and the structure of inelastic constitutive laws, SIAM J. Appl. Math. 25, 448-461.

Holcomb, D. J., and W. A. Olsson (2003), Compaction localization and fluid flow, *J. Geophys. Res., 108, 2290,* doi:10.1029/2001JB000813.

Holcomb, D., and J. Rudnicki (2001), Inelastic constitutive properties and shear localization in Tennessee marble, *Int. J. Numerical Analytical Methods Geomechanics, 25,* 109-129.

Holcomb, D., W. Olsson, and J. Rudnicki (2004), Compaction localization: effects on permeability and reservoir mechanics, paper presented at AAPG Hedberg Conference, Austin, TX.

Holcomb, D., J. Rudnicki, K. Issen, and K. Sternlof (2007), Compaction localization in the earth and the laboratory: state of the research and research directions, *Acta Geotechnica 2,* 1-15.

Ingraham, M.D., Issen, K.A., and Holcomb, D. (2013a), Use of acoustic emissions to investigate localization in high-porosity sandstone subjected to true triaxial stress, *Acta Geotechnica* 8, 645-663.

Ingraham, M.D., Issen, K.A., and Holcomb, D. (2013b), Response of Castlegate sandstone to true triaxial states of stress, *J. Geophys. Res., 118,*536-552, doi:10.1002/jgrb.50084.

Issen, K.A. (2002), The influence of constitutive models on localization conditions for porous rock, *Eng. Fracture Mech., 69,* 1891-1906.

Issen, K.A. and Challa, V. (2008), Influence of the intermediate principal stress on the strain localization mode in porous sandstone, *Journal of Geophysical Research, 113(B02103)*: doi:10.1029/2005JB004008.

Issen, K.A., and J.W. Rudnicki (2000), Conditions for compaction bands in porous rock, *J. Geophys. Res., 105,* 21529-21536.

Issen, K.A., and J.W. Rudnicki (2001), Theory of compaction bands in porous rock, *Phys. Chem. Earth (A), 26(1-2),* 95-100.

Karner, S., J. Chester, F. Chester, A. Kronenberg, and A. Hajash (2005), Laboratory deformation of granular quartz sand: Implications for the burial of clastic rocks, *Am. Assoc. Petrol. Geologists Bull. 89 (5),* 603-625.

Karner, S., F. Chester, A. Kronenberg, and J. Chester (2003), Subcritical compaction and yielding of granular quartz sand, *Tectonophysics, 377,* 357-381.

Khan, A., Y. Xiang, and S. Huang (1991), Behavior of Berea Sandstone under confining pressure Part I: Yield and failure surfaces, and nonlinear elastic response, *Int. J. Plasticity, 7,* 607-624.

Klein, E., P. Baud, T. Reuschle, and T-f. Wong (2001), Mechanical behaviour and failure mode of Bentheim sandstone under triaxial compression, *Phys. Chem. Earth (A), 26,* 21–25.

McLaurin, B.T. and R.J. Steel (2007), Architecture and origin of an amalgamated fluvial sheet sand, lower Castlegate Formation, Book Cliffs, Utah, *Sedimentary Geology, 197*, 291-311.

Mollema, P. N., and M. A. Antonellini (1996), Compaction bands: A structural analog for anti-mode I cracks in aeolian sandstone, *Tectonophysics*, *267*, 209–228.

Muhuri, S.K. (1994), Experimental and Microscopic Study of the Transition From Brittle to Ductile Behavior in the Porous Berea Sandstone as a Function of Confining Pressure. M.S. thesis, University of Oklahoma, Norman, Oklahoma.

Olsson, W. A. (2001), Quasistatic propagation of compaction fronts in porous rock, *Mech. Mat.*, *33*, 659-668.

Olsson, W. A. (1999), Theoretical and experimental investigation of compaction bands in porous rock, *J. Geophys. Res.*, *104*, 7219-7228.

Olsson, W. A., and D. J. Holcomb (2000), Compaction localization in porous rock, *Geophys. Res. Letters*, *27*, 3537–3540.

Olsson, W., D.J. Holcomb, and J. Rudnicki (2002), Compaction localization in porous sandstone: Implications for Reservoir Mechanics, *Oil and Gas Science and Technology, Rev. IFP 57*, 591-599.

Rudnicki J.W. (1984), A class of elastic-plastic constitutive laws for brittle rock, *Journal of Rheology, 28(6)*, 759-778.

Rudnicki, J. (2004), Shear and compaction band formation on an elliptic yield cap, *J. Geophysical Research, 109,* B03402.

Rudnicki, J. (2007), Extension of compaction bands in porous sandstones. Euro-conference of Rock Physics and Geomechanics on Natural Hazards: Thermo-Hydro-Mechanical Processes in Rocks, Erice, Italy.

Rudnicki, J.W., and J.R. Rice (1975). Conditions for the localization of deformation in pressure sensitive dilatant materials. *J. Mech. Phys. Solids*, *23,* 371-394.

Rudnicki, J. W., and W.A. Olsson (1998), Reeaxmination of Fault Angles Predicted by Shear Localization Theory, *Int. J. Rock Mech. Min. Sci*. *35*, 512-513.

Rutqvist J., D. Vasco, and L. Myer (2009), Coupled reservoir-geomechanical analysis of CO2 injection and ground deformations at In Salah, Algeria, *Int. J. Greenhouse Gas Control,* doi:10.1016/j.ijggc.2009.10.017.

Stanchits, S., J. Fortin, Y. Gueguen, and G. Dresen (2007), Initiation and propagation of compaction bands in dry and wet sandstone. Euro-conference of Rock Physics and Geomechanics on Natural Hazards: Thermo-Hydro-Mechanical Processes in Rocks, Erice, Italy.

Sternlof, K.R., J.R. Chapin, D.D. Pollard, and L.J. Durlofsky (2004), Permeability effects of deformation band arrays in sandstone: *AAPG Bulletin, 88*, 1315-1329.

Sulem, J., and H. Ouffroukh (2006), Hydromechanical behaviour of Fountainebleau Sandstone, *Rock Mechanics Rock Engineering, 39 (3),* 185-213.

Sulem, J., I. Vardoulakis, E. Papamichos, A. Oulahna, and J. Tronvoll (1999), Elasto-plastic modeling of Red Wildmoor sandstone, *Mechanics of Cohesive-Frictional Materials, 4,* 215-245.

Tembe, S., V. Vajdova, T.-f. Wong, and W. Zhu (2006), Initiation and propagation of strain localization in circumferentially notched samples of two porous sandstones, *J. Geophys. Res., 111,* B02409,doi:10.1029/2005JB003611.

Tembe, S., Vajdova, V., Baud, P., Zhu, W., and Wong, T.-f. (1997), A new methodology to delineate the compactive yield cap for two porous sandstones under undrained condition. *Mechanics of Materials*, *39*, 513-523.

Vajdova, V., P. Baud, P., and T.-f, Wong (2004), Permeability evolution during localized deformation in Bentheim sandstone, *J. Geophys. Res.*, *109*, B10406, doi:10.1029/2003JB002942.

Vinegar, H., J. DeWaal, and S. Wellington (1991), CT studies of brittle failure in Castlegate Sandstone. *Int. J. Rock Mechanics Mining Sciences & Geomech. Abstracts 28*, 441-448.

Wawersik, W. R., J. W. Rudnicki, P. Dove, J. Harris, J. M. Logan, L. Pyrak-Nolte, F. M. Orr, P. J. Ortoleva, F. Richter, N. R. Warpinski, J. L. Wilson, and T.-f. Wong (2000), Terrestrial sequestration of CO2: An assessment of research needs, *Advances in Geophysics, 43,* 97-177.

Wong, T.-f., H. Szeto, and J. Zhang (1992), Effect of loading path and porosity on the failure mode of porous rocks. *Appl. Mech. Rev., 45*(8), 281-293.

Wong, T.-f., C. David, and W. Zhu (1997), The transition from brittle faulting to cataclastic flow in porous sandstones: Mechanical deformation. *J. Geophysical Research, 102*, 3009-3025.

Wong, T-f., Baud, P., and E. Klein (2001), Localized failure modes in a compactant porous rock, *Geophys. Res. Lett.*, *28*, 2521–2524.

Zhang, J., T.-f. Wong, and D. Davis (1990), Micromechanics of pressure-induced grain crushing in porous rocks, *Journal of Geophysical Research*, *95*, 341-352.

Figure Captions

Figure 1. Idealized yield surface in space of Mises equivalent shear stress τ and mean stress σ. Also delineated is a portion of the plastic potential, and definitions of the constitutive parameters β and μ. The vertically oriented arrow normal to the plastic potential surface refers to the direction of inelastic increment of strain as defined in the text. The dashed arrow shows the loading path in stress space.

Figure 2. **A** and **B**. Axial and radial stress-strain pathways shown for Castlegate experiments exhibiting localization (**A**) and no localization (**B**). Curves on the right hand side of plots correspond to axial strains; those on the left correspond to radial strains. **C** and **D**. Loading pathways in $\sigma - \tau$ space are shown for uniaxial, triaxial, and constant mean stress experiments for samples with localization (**C**) and no localization (**D**).

Figure 3. Castlegate axial stress-strain curves with acoustic emissions for **A**. uniaxial loading path resulting in shear localization (experiment 41); **B**. constant mean stress loading (experiment 22) resulting in shear localization; **C.** constant mean stress loading (experiment 15) resulting in compaction localization; and **D.** constant mean stress loading path (experiment 21) resulting in spatially pervasive pore collapse.

Figure 4. Acoustic Emissions (AE) results for specimen 22 (shear localization). The lower panel shows axial stress (thin black line) and calculated band angle (thick gray line) vs. axial strain. In the upper panel, acoustic emissions events (black and gray dots) are shown for three portions of the test indicated by the arrows. Only the black dot events were used to calculate the band angle.

Figure 5. AE results for specimen 15 (compaction localization) . The lower panel shows axial stress (thin black line) and calculated band angle (thick gray line) vs. axial strain. In the upper panel, acoustic emissions events (black and gray dots) are shown for three portions of the test indicated by the arrows. Only the black dot events were used to calculate the band angle.

Figure 6. AE results for specimen 21 (no localization). The lower panel shows axial stress (thin black line) and calculated band angle (thick gray line) vs. axial strain. In the upper panel, acoustic emissions events (black and gray dots) are shown for three portions of the test indicated by the arrows.

Figure 7. **A**. Mean stress-volume strain path for hydrostatic compression experiment 38, including four unloading loops and final unloading. **B**. Observed (symbols) and model prediction (solid line) of tangent bulk modulus evolution for experiment 38, including both mean stress and plastic volume strain dependence. The solid grey line is the calculated secant bulk modulus. **C**. Partitioning of total volume strain in A (solid black line) into elastic (solid dark grey line) and plastic (dashed black line) portions. The light grey curve shows the elastic response ignoring elastic-plastic coupling. Nearly half of the total strain arises from elastic-plastic coupling, i.e., the plastic volume strain dependence of the bulk modulus. **D**. Evolution of the K_0 parameter for the bulk modulus model, used to quantify the modulus degradation due to plastic volume strain dependence.

Figure 8. **A**. Measured shear stress-strain plot for Castlegate sandstone (experiment 42) deformed at a constant mean stress of 140 MPa. **B**. Observed tangent shear moduli (symbols) and model prediction (solid line) of shear modulus evolution for experiment 42, including stress and plastic shear strain-dependence. **C**. Partitioning of total measured shear strain in A (solid black line) into elastic (solid dark grey line) and plastic (dashed black line) portions. The light grey curve shows the elastic response ignoring elastic-plastic coupling. In this case, about 20% of the total strain arises from elastic-plastic coupling, i.e., the plastic shear strain dependence of the shear modulus. **D**. Evolution of the G_0 parameter for the shear modulus model, used to quantify the modulus degradation due to plastic shear strain dependence.

Figure 9. Partitioning of total measured strain (black curves) into elastic (dark grey line) and plastic (dashed black line) portions for three Castlegate experiments, shown as mean stress vs. volume strain, and shear stress vs. shear strain: **A** and **B.** Experiment 41; **C.** and **D.** Experiment 22; **E. & F.,** Experiment 15. The light grey curve in all cases shows the calculated elastic strain if elastic-plastic coupling is ignored.

Figure 10. **A.** τ -σ plots contoured for constant inelastic shear strain. This includes both total plastic strain and that due to elastic plastic coupling and is equal to the sum of the inelastic increment of shear strain. Plotted are data from experiments 41, 22, 20, 15, and 21. Inelastic shear strain contour values are equal to the value at peak for each individual experiment. **B.** $\sigma - \tau$ plots contoured for inelastic volume strain (sum of inelastic increments of volume strain, which includes plastic volume strain and that due to elastic plastic coupling). Includes data from experiments 14, 15, and 21. Also shown as dashed line in both **A** and **B** is the failure surface: the locus of peak yield stresses for experiments that localized are shown as solid squares in **A**.

Figure 11. A. Plot of inelastic volume strain ${}^{p}\varepsilon$ versus inelastic shear strain ${}^{p}\gamma$, for all axisymmetric triaxial compression experiments performed with Castlegate sandstone. The constitutive parameter β is determined as the negative of the local slopes of these curves. Experiments that resulted in shear localization have positive values of β, while those that experienced compaction localization have negative β.

Tables

Table 1. Summary of experiments, including loading configuration, stress conditions, peak stresses, and failure mode

Experiment	Loading type	σ	Peak σ_3[1]	Peak σ_1[1]	Maximum σ[1]	Maximum τ[1]	Localization mode
38	hydrostatic	-	400	400	400	-	
41	uniaxial	0	0	14.5	4.9	8.4	shear band
40	uniaxial	0	0	14.4	4.8	8.4	shear band
22	constant σ	25	8.5	56	25	28	shear band
20	constant σ	30	11	68	30	32	shear band
14	constant σ	50	26	98	50	42	low-angle shear b.
15	constant σ	70	41	127	70	52	compactional band
21	constant σ	90	60	150	90	56	no banding
23	constant σ	110	83	160	110	58	no banding
42	constant σ	150	110	233	150	72	no banding
44	constant σ	185	143	266	185	73	no banding
43	constant σ	195	150	284	195	77	no banding
13	triaxial	45	45	123	71	45	compactional band
17	triaxial	45	45	121	70	43	compactional band
8	triaxial	45	45	132	74	50	compactional band
3	triaxial	50	50	137	79	51	compactional band
16	triaxial	45	45	125	71	46	compactional band

Notes:

[1] Mpa

Table 2. Summary of pre-peak constitutive parameters and calculated angles

Shear Surface							
Exper#	β	μ	ν	G^1	h_{cr}/G	θ, predicted^2	θ, observed^2
41	0.92	1.23	0.23	1267	-1.01	73	67-70
40	1.01	1.23	0.23	1635	-1.07	76	67-69
22	0.17	0.68	0.16	2410	-0.39	49	30-35
20	0.26	0.63	0.15	4885	-0.42	50	45-48
14	-0.23	0.35	0.17	5273	-0.17	40	8-12
13	-0.58	0.26	0.20	4424	-0.22	35	10-20
15	-0.41	0.26	0.18	4598	-0.32	37	4-8; 5-25
17	-0.59	0.26	0.21	4528	-0.21	35	5-8; 19-20
21	-0.51	0.20	0.18	5912	-0.24	35	no local.
Cap Surface							
Exper#	β	μ	ν	G^1	k_{cr}/G	θ, predicted^2	θ, observed^2
14	-0.23	-0.82	0.17	5273	0.131	23	8-12
13	-0.58	-1.02	0.20	4424	0.051	10	10-20
15	-0.41	-1.02	0.18	4598	0.108	15	4-8; 5-25
17	-0.59	-1.02	0.21	4528	0.049	10	5-8; 19-20
21	-0.51	-0.88	0.18	5912	0.007	16	no local.
Notes: ^{1}MPa ^{2}degrees							

Figure 1

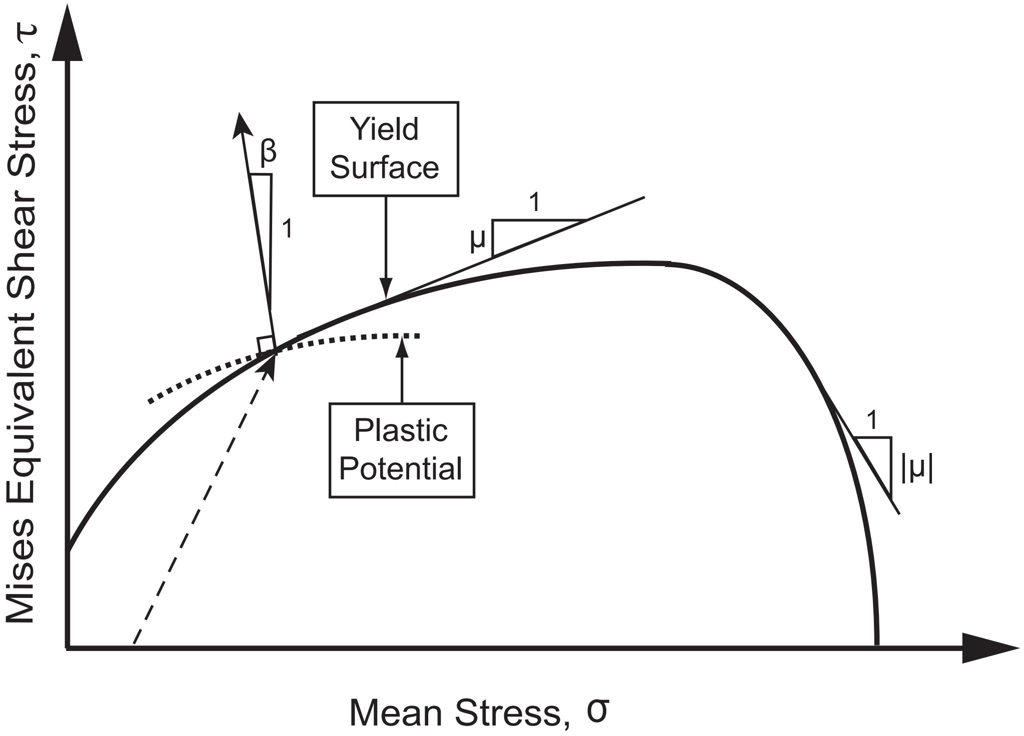
Mises Equivalent Shear Stress, τ
Mean Stress, σ
β
1
Yield Surface
1
μ
Plastic Potential
1
|μ|

Figure 2

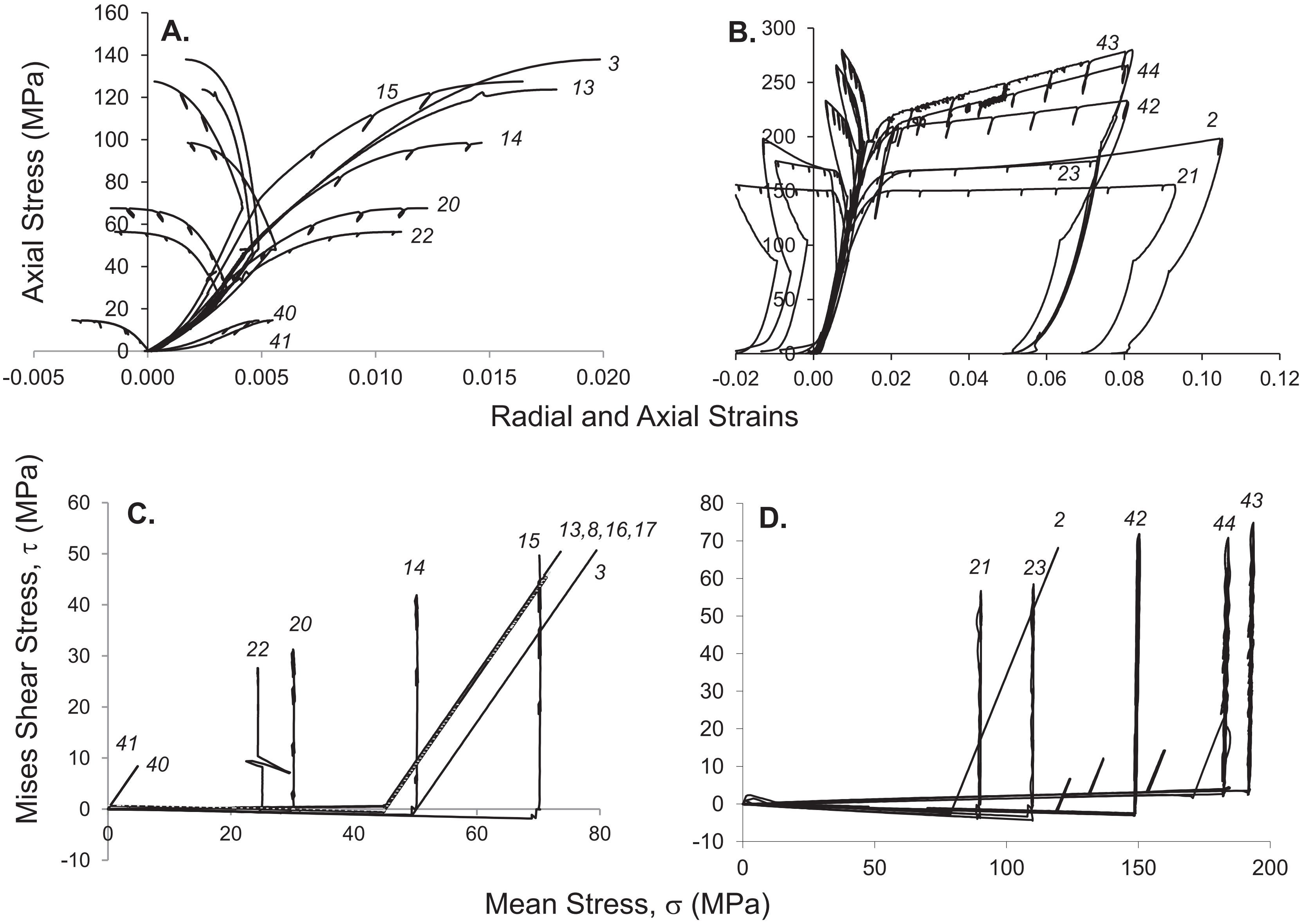
A.
Axial Stress (MPa)
160
140
120
100
80
60
40
20
0
-0.005
0.000
0.005
0.010
0.015
0.020
3
13
15
14
20
22
40
41
B.
300
250
200
150
100
50
0
-0.02
0.00
0.02
0.04
0.06
0.08
0.10
0.12
43
44
42
2
23
21
Radial and Axial Strains
C.
Mises Shear Stress, τ (MPa)
60
50
40
30
20
10
0
-10
0
20
40
60
80
15
13,8,16,17
3
14
20
22
41
40
D.
80
70
60
50
40
30
20
10
0
-10
0
50
100
150
200
2
42
43
44
21
23
Mean Stress, σ (MPa)

Figure 3

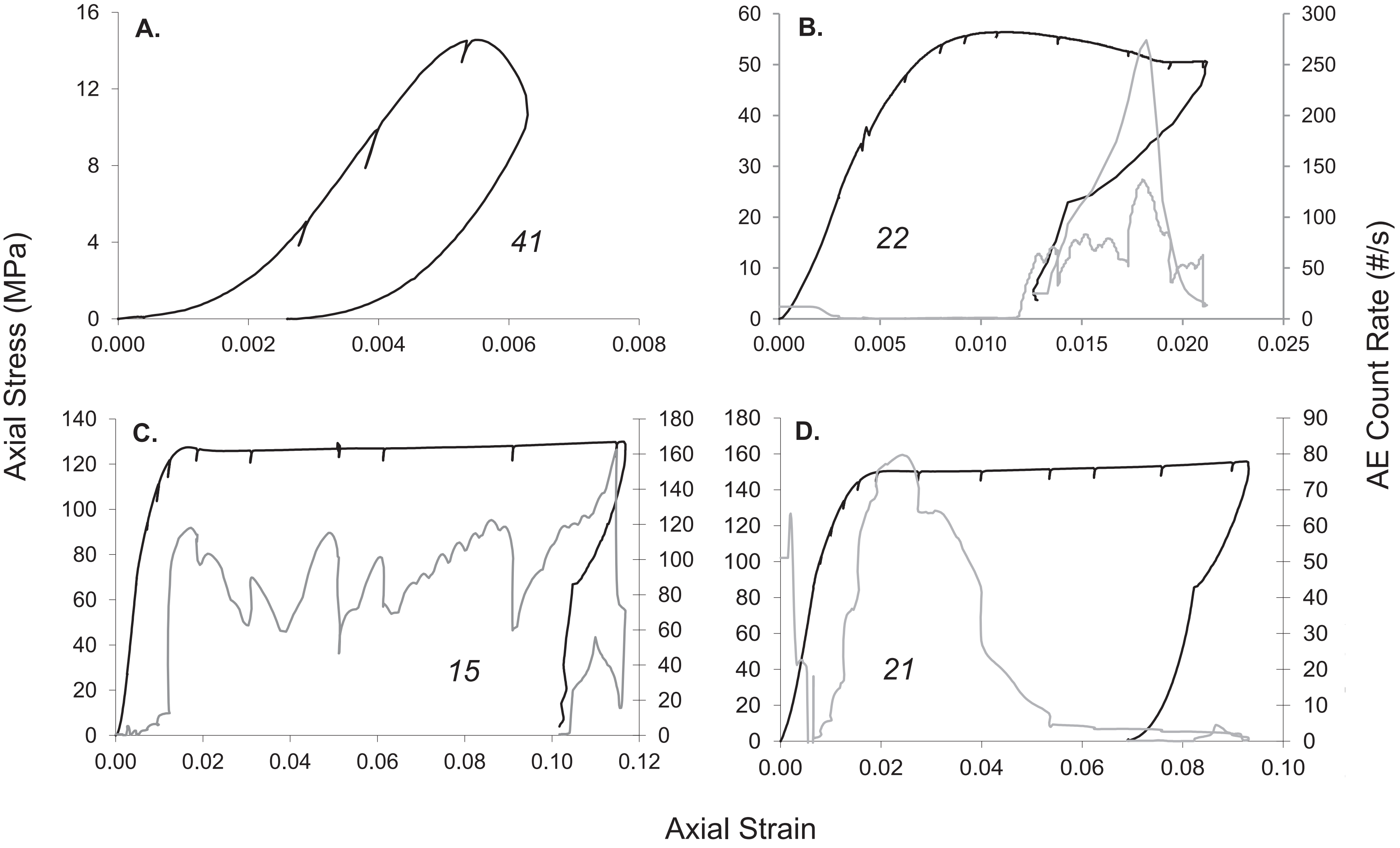

A.
B.
C.
D.
41
22
15
21
Axial Stress (MPa)
AE Count Rate (#/s)
Axial Strain
0
4
8
12
16
0.000
0.002
0.004
0.006
0.008
0
10
20
30
40
50
60
0.000
0.005
0.010
0.015
0.020
0.025
0
50
100
150
200
250
300
0
20
40
60
80
100
120
140
0.00
0.02
0.04
0.06
0.08
0.10
0.12
0
20
40
60
80
100
120
140
160
180
0
20
40
60
80
100
120
140
160
180
0.00
0.02
0.04
0.06
0.08
0.10
0
10
20
30
40
50
60
70
80
90

Figure 4

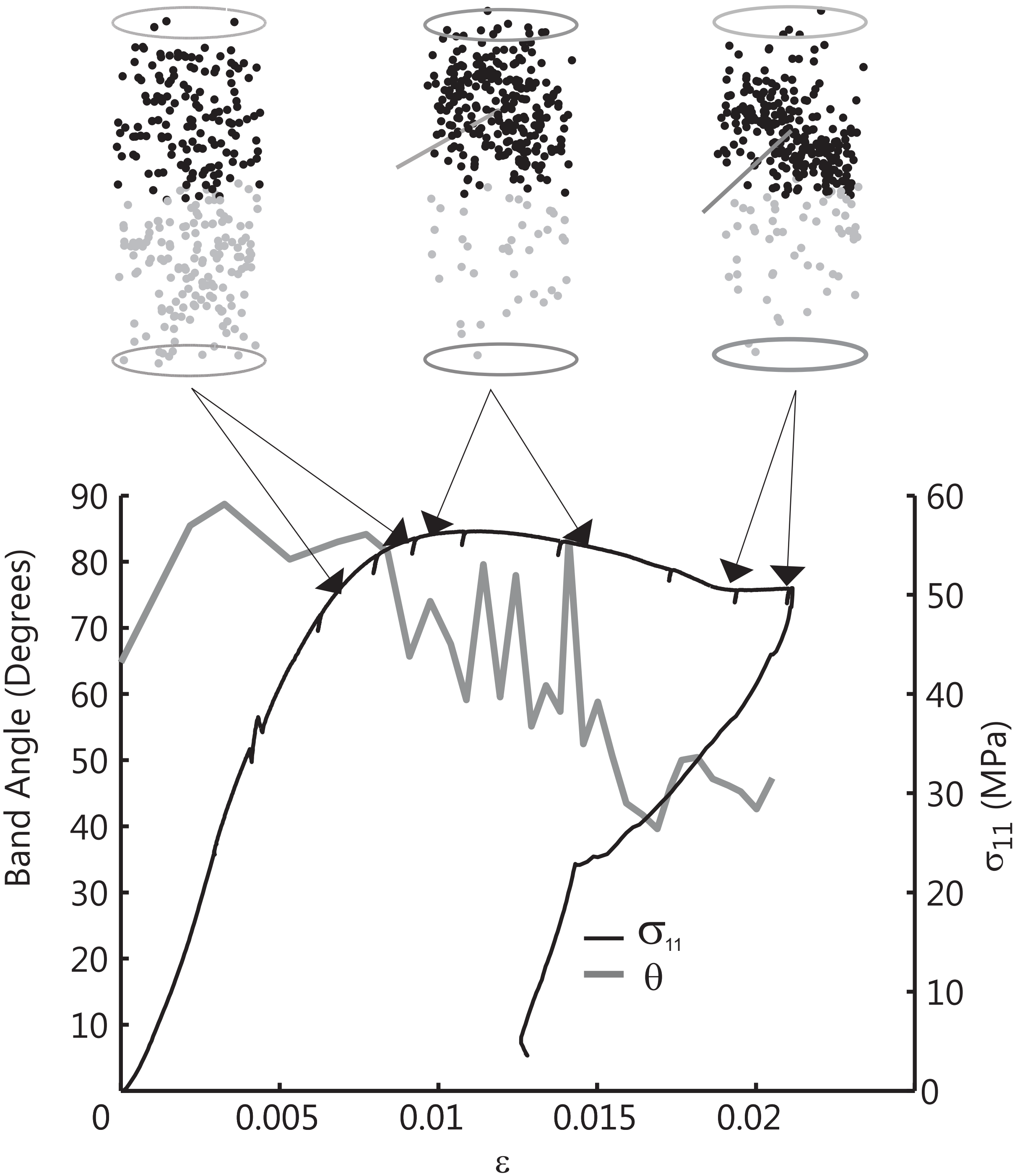
Band Angle (Degrees)
0
10
20
30
40
50
60
70
80
90
σ11 (MPa)
0
10
20
30
40
50
60
0
0.005
0.01
0.015
0.02
ε_{11}
σ_{11}
θ

Figure 5

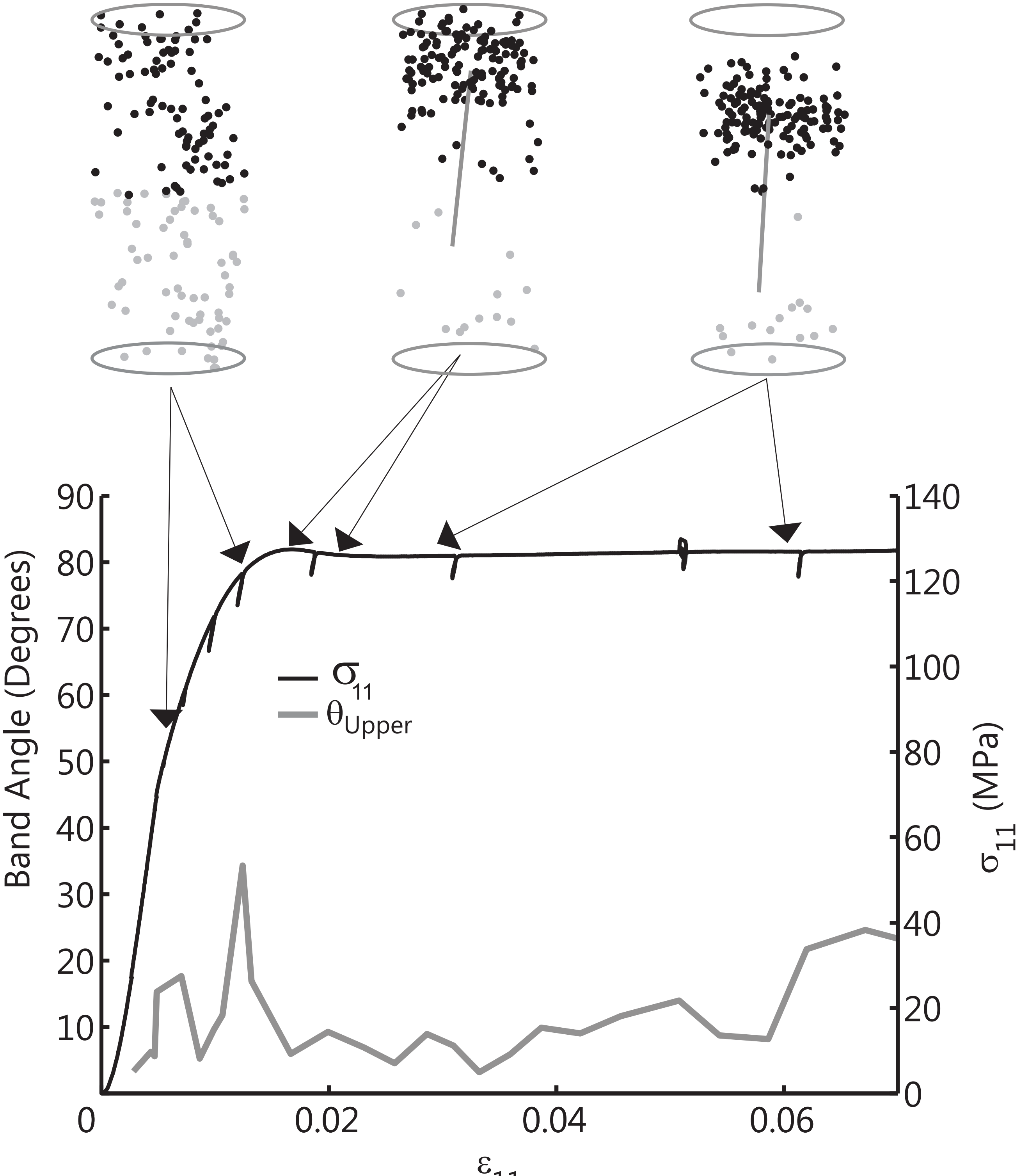

σ11
θUpper
Band Angle (Degrees)
σ11 (MPa)
ε11
0
10
20
30
40
50
60
70
80
90
0
20
40
60
80
100
120
140
0
0.02
0.04
0.06

Figure 6

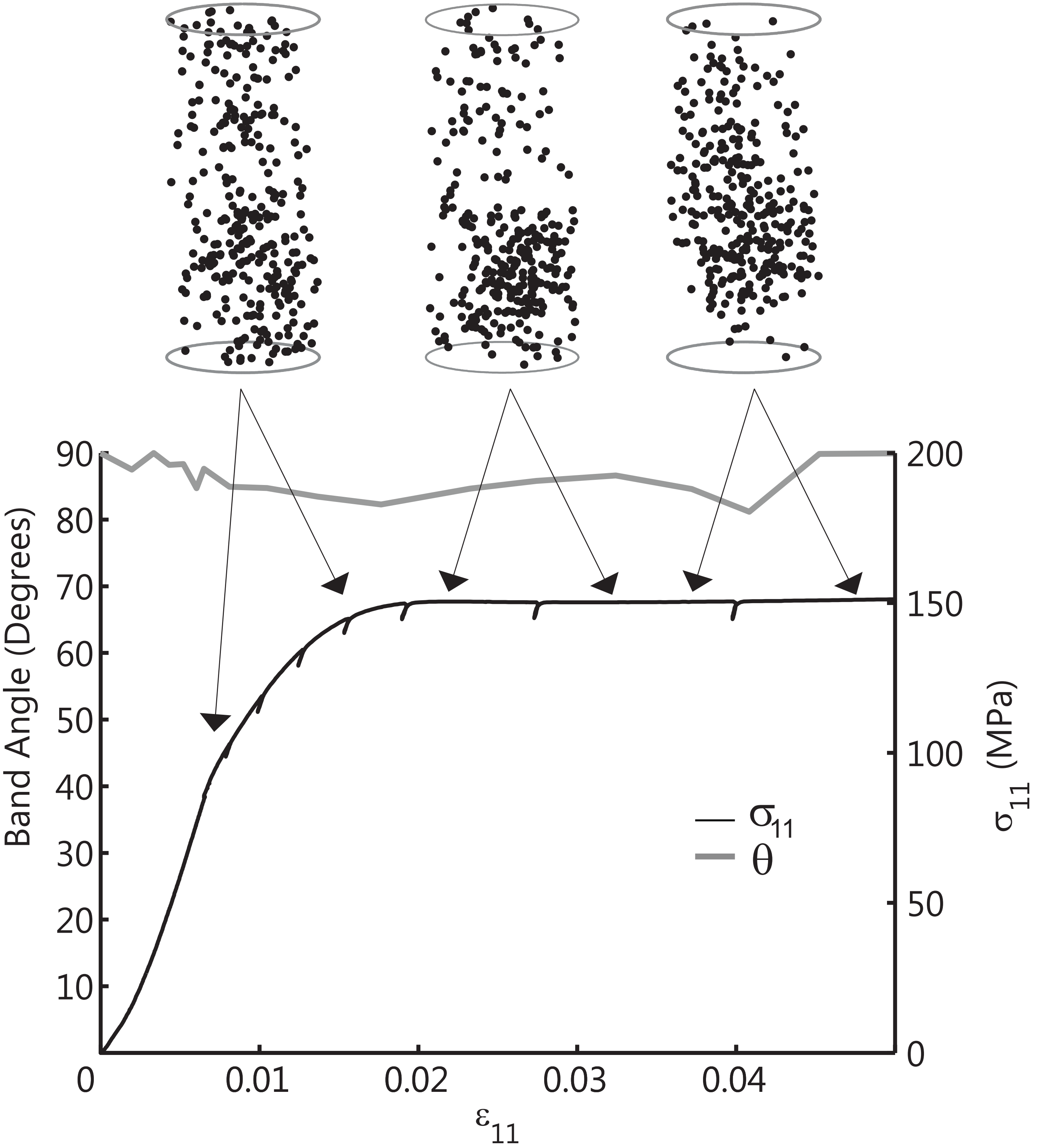

Band Angle (Degrees)
90
80
70
60
50
40
30
20
10
0
0.01
0.02
0.03
0.04
ε_{11}
200
150
100
50
0
σ_{11} (MPa)
σ_{11}
θ

Figure 7

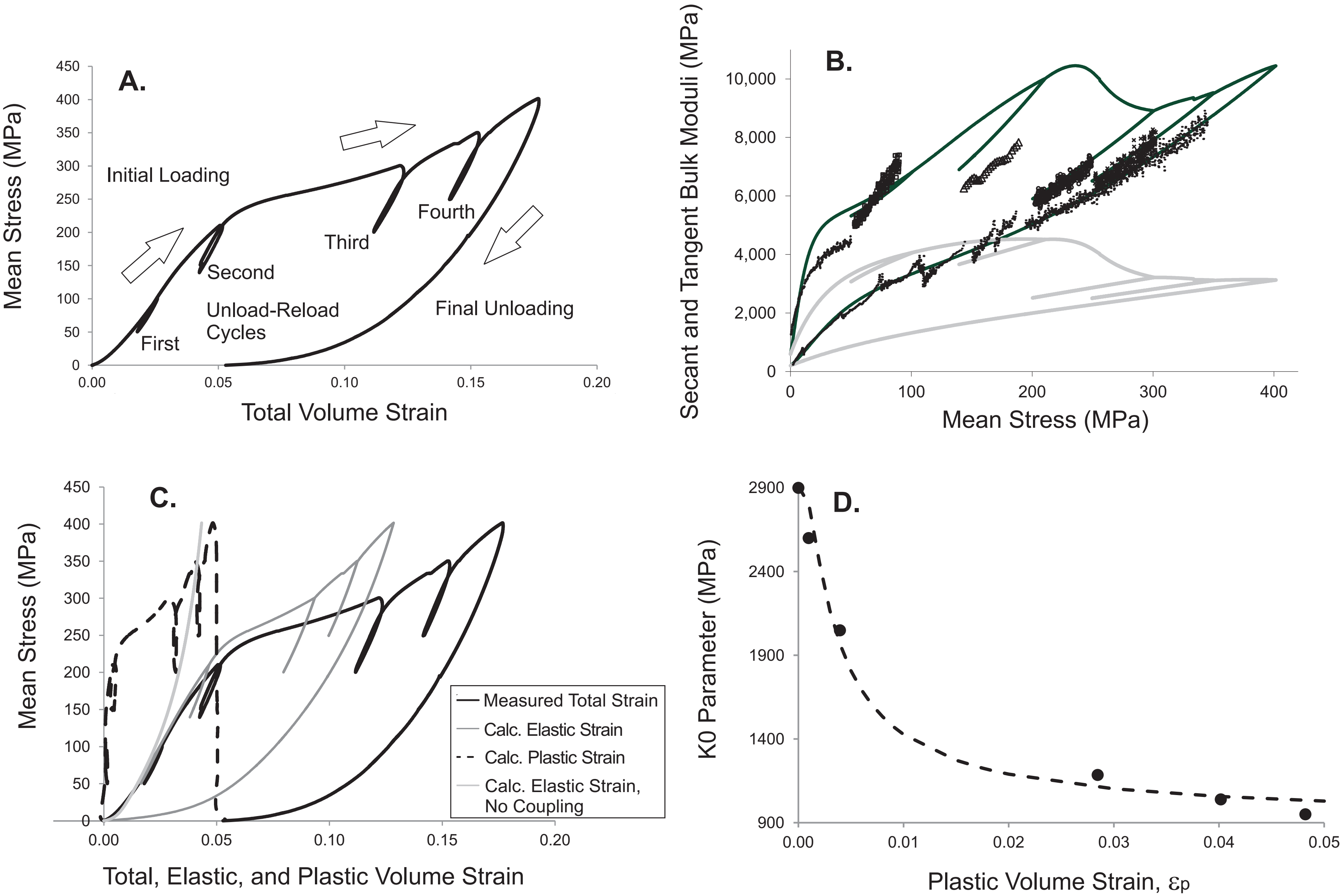
A.
Mean Stress (MPa)
0
50
100
150
200
250
300
350
400
450
Total Volume Strain
0.00
0.05
0.10
0.15
0.20
Initial Loading
First
Second
Third
Fourth
Unload-Reload
Cycles
Final Unloading
B.
Secant and Tangent Bulk Moduli (MPa)
0
2,000
4,000
6,000
8,000
10,000
Mean Stress (MPa)
0
100
200
300
400
C.
Mean Stress (MPa)
0
50
100
150
200
250
300
350
400
450
Total, Elastic, and Plastic Volume Strain
0.00
0.05
0.10
0.15
0.20
Measured Total Strain
Calc. Elastic Strain
Calc. Plastic Strain
Calc. Elastic Strain, No Coupling
D.
K0 Parameter (MPa)
900
1400
1900
2400
2900
Plastic Volume Strain, εp
0.00
0.01
0.02
0.03
0.04
0.05

Figure 8

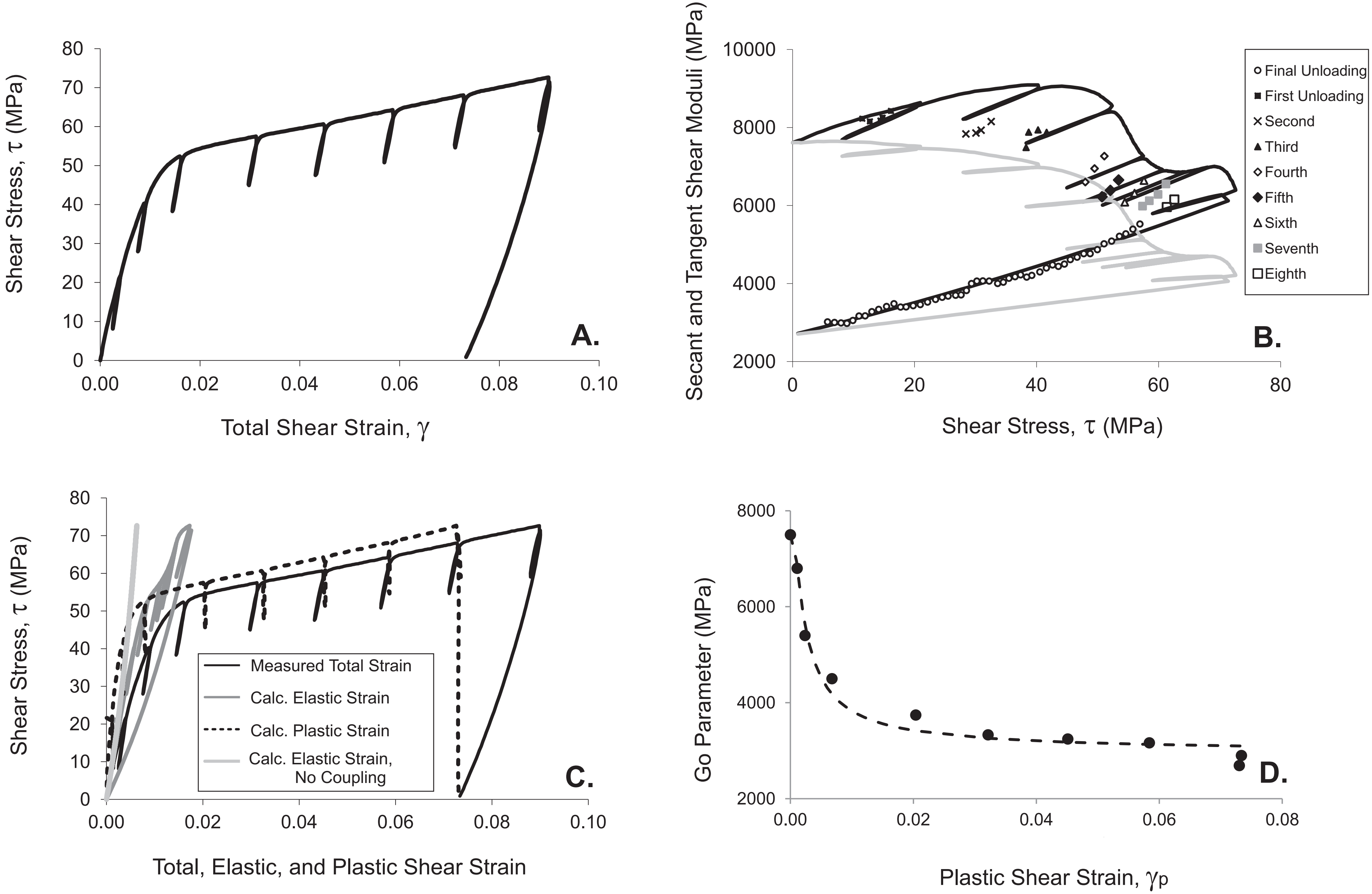
A.
Shear Stress, τ (MPa)
0
10
20
30
40
50
60
70
80
0.00
0.02
0.04
0.06
0.08
0.10
Total Shear Strain, γ
B.
Secant and Tangent Shear Moduli (MPa)
2000
4000
6000
8000
10000
0
20
40
60
80
Shear Stress, τ (MPa)
○ Final Unloading
■ First Unloading
× Second
▲ Third
◇ Fourth
◆ Fifth
△ Sixth
■ Seventh
□ Eighth
C.
Shear Stress, τ (MPa)
0
10
20
30
40
50
60
70
80
0.00
0.02
0.04
0.06
0.08
0.10
Total, Elastic, and Plastic Shear Strain
Measured Total Strain
Calc. Elastic Strain
Calc. Plastic Strain
Calc. Elastic Strain, No Coupling
D.
Go Parameter (MPa)
2000
4000
6000
8000
0.00
0.02
0.04
0.06
0.08
Plastic Shear Strain, γp

Figure 9

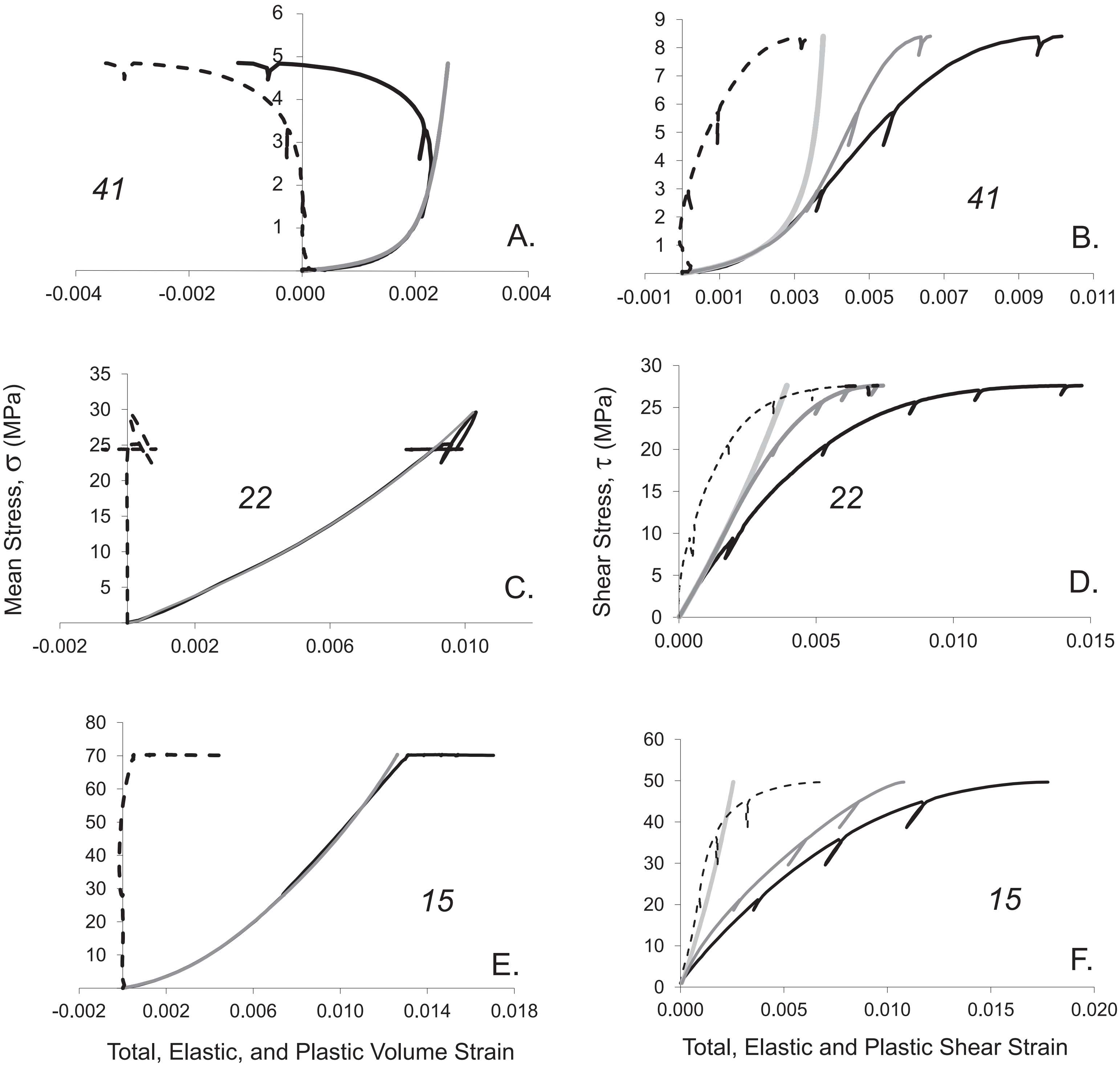

A.
41
6
5
4
3
2
1
-0.004
-0.002
0.000
0.002
0.004
B.
41
9
8
7
6
5
4
3
2
1
-0.001
0.001
0.003
0.005
0.007
0.009
0.011
C.
22
Mean Stress, σ (MPa)
35
30
25
20
15
10
5
-0.002
0.002
0.006
0.010
D.
22
Shear Stress, τ (MPa)
30
25
20
15
10
5
0
0.000
0.005
0.010
0.015
E.
15
80
70
60
50
40
30
20
10
-0.002
0.002
0.006
0.010
0.014
0.018
Total, Elastic, and Plastic Volume Strain
F.
15
60
50
40
30
20
10
0
0.000
0.005
0.010
0.015
0.020
Total, Elastic and Plastic Shear Strain

Figure 10

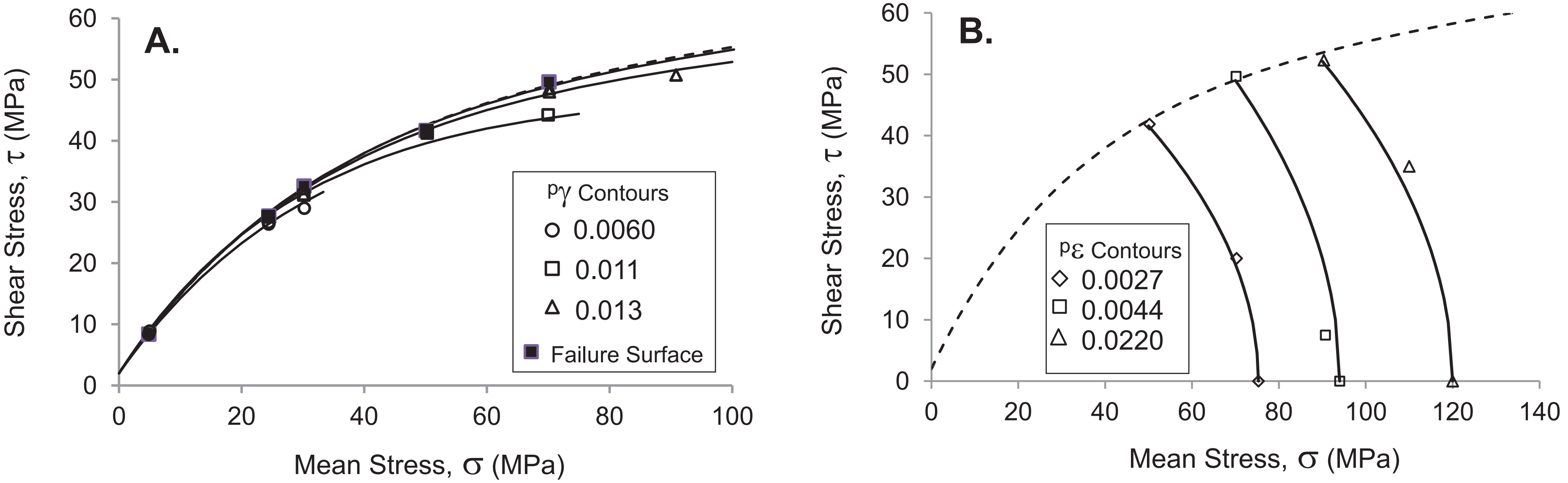
A.
Shear Stress, τ (MPa)
Mean Stress, σ (MPa)
0
10
20
30
40
50
60
0
20
40
60
80
100
pγ Contours
○ 0.0060
□ 0.011
△ 0.013
■ Failure Surface
B.
Shear Stress, τ (MPa)
Mean Stress, σ (MPa)
0
10
20
30
40
50
60
0
20
40
60
80
100
120
140
pε Contours
◇ 0.0027
□ 0.0044
△ 0.0220

Figure 11

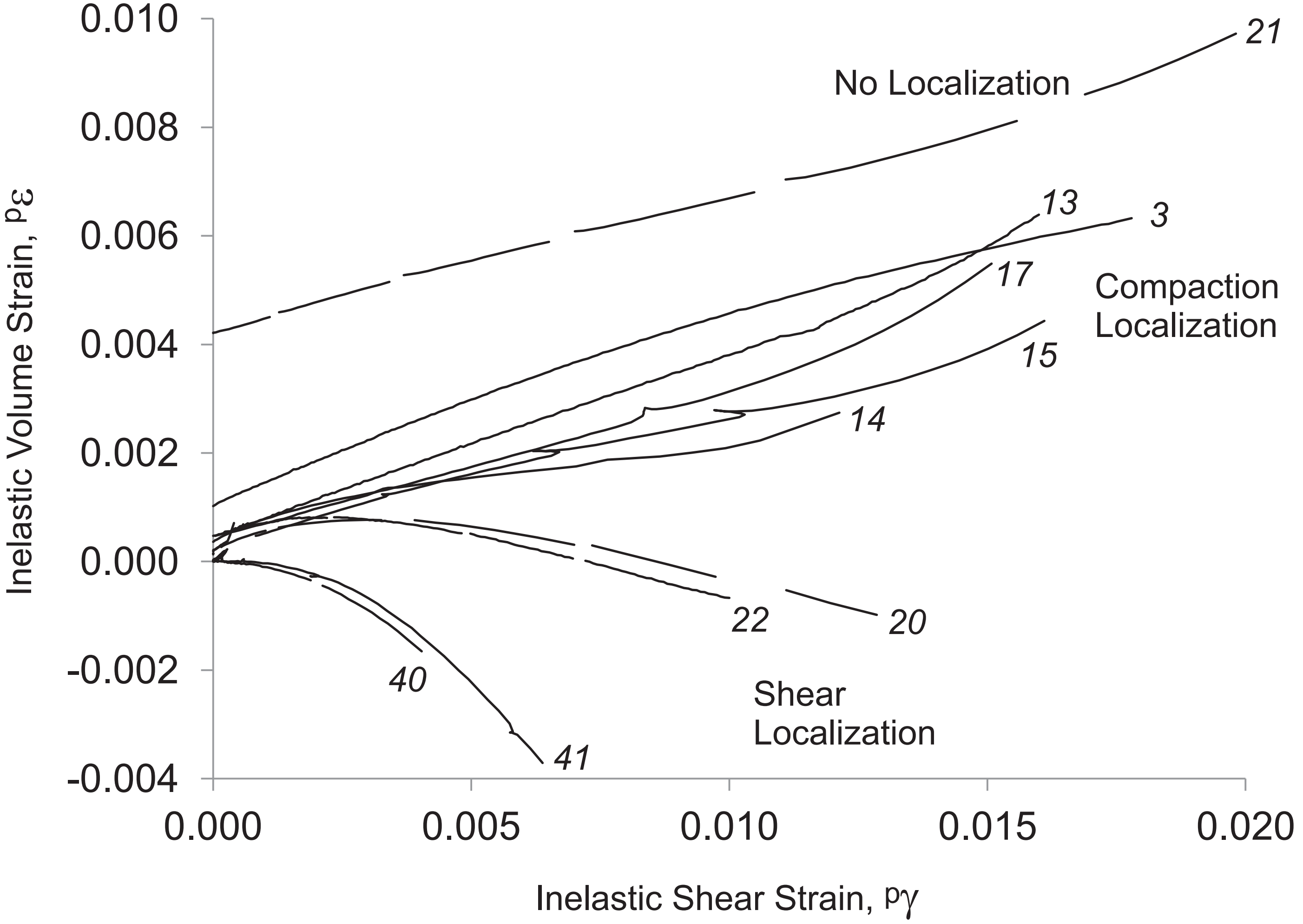

0.010
0.008
0.006
0.004
0.002
0.000
-0.002
-0.004
0.000
0.005
0.010
0.015
0.020
Inelastic Volume Strain, $^p\varepsilon$
Inelastic Shear Strain, $^p\gamma$
No Localization
21
13
3
17
15
14
Compaction Localization
22
20
40
41
Shear Localization